



BNL-211572-2019-JAAM

# Synergistic Metal-Ligand Redox Cooperativity for Electrocatalytic CO<sub>2</sub> Reduction Promoted by a Ligand-Based Redox Couple in Mn and Re Tricarbonyl Complexes

M. McKinnon, D. C. Grills

To be published in "ORGANOMETALLICS"

March 2019

Chemistry Department  
**Brookhaven National Laboratory**

**U.S. Department of Energy**  
USDOE Office of Science (SC), Basic Energy Sciences (BES) (SC-22)

Notice: This manuscript has been authored by employees of Brookhaven Science Associates, LLC under Contract No. DE-SC0012704 with the U.S. Department of Energy. The publisher by accepting the manuscript for publication acknowledges that the United States Government retains a non-exclusive, paid-up, irrevocable, world-wide license to publish or reproduce the published form of this manuscript, or allow others to do so, for United States Government purposes.

## **DISCLAIMER**

This report was prepared as an account of work sponsored by an agency of the United States Government. Neither the United States Government nor any agency thereof, nor any of their employees, nor any of their contractors, subcontractors, or their employees, makes any warranty, express or implied, or assumes any legal liability or responsibility for the accuracy, completeness, or any third party's use or the results of such use of any information, apparatus, product, or process disclosed, or represents that its use would not infringe privately owned rights. Reference herein to any specific commercial product, process, or service by trade name, trademark, manufacturer, or otherwise, does not necessarily constitute or imply its endorsement, recommendation, or favoring by the United States Government or any agency thereof or its contractors or subcontractors. The views and opinions of authors expressed herein do not necessarily state or reflect those of the United States Government or any agency thereof.

# Synergistic metal-ligand redox-cooperativity for electrocatalytic $\text{CO}_2$ reduction promoted by a ligand-based redox couple in Mn and Re tricarbonyl complexes

Meaghan McKinnon<sup>†</sup>, Ken T. Ngo<sup>†</sup>, Sebastian Sobottka<sup>‡</sup>, Biprajit Sarkar<sup>‡</sup>, Mehmed Z. Ertem<sup>\*\*</sup>, David C. Grills<sup>\*\*</sup> and Jonathan Rochford<sup>†\*</sup>

<sup>†</sup>Department of Chemistry, University of Massachusetts Boston, 100 Morrissey Boulevard, Boston, MA 02125,

USA. <sup>‡</sup>Institut für Chemie und Biochemie, Anorganische Chemie, Freie Universität Berlin, Fabeckstrasse 34-36, Berlin, Germany. <sup>\*\*</sup>Chemistry Division, Brookhaven National Laboratory, Upton, NY, 11973-5000, USA.

## Supporting Information Placeholder

**ABSTRACT:** Electrocatalytic  $\text{CO}_2$  reduction is demonstrated for the Mn and Re tricarbonyl complexes,  $[\text{M}(\text{Me}_2\text{OQN})(\text{CO})_3(\text{CH}_3\text{CN})]$  ( $\text{M} = \text{Mn}$  or  $\text{Re}$ ) containing the 5,7-dimethyl-8-oxyquinolate ( $\text{Me}_2\text{OQN}^-$ ) ligand. In comparison to the related 2,2'-bipyridyl (bpy) reference complexes,  $[\text{M}(\text{bpy})(\text{CO})_3(\text{CH}_3\text{CN})]^+$  ( $\text{M} = \text{Mn}$  or  $\text{Re}$ ), the  $\text{Me}_2\text{OQN}^-$ -based pre-catalysts exhibit onset of catalytic current with the input of one less equivalent of electrons. This behavior is attributed to the formal  $\text{Me}_2\text{OQN}^{(\bullet-)}$  redox couple which contributes towards each catalytic cycle in tandem with the formal  $\text{Mn}^{(\text{I}/\text{O})}$  and  $\text{Re}^{(\text{I}/\text{O})}$  redox couples. In addition to computational support for synergistic metal-ligand redox-cooperativity, electrochemistry (cyclic voltammetry and controlled potential electrolysis), spectroelectrochemistry (FTIR and EPR), and pulse radiolysis coupled with time-resolved infrared (TRIR) spectroscopy, provide structural insight into the electronic properties of the one-electron and two-electron reduced species.

## INTRODUCTION

The harvesting and storage of solar energy in the form of chemical bonds via electrocatalytic  $\text{CO}_2$  conversion with solar-derived electricity is highly desired. Of the many classes of homogeneous transition metal catalysts investigated for  $\text{CO}_2$  reduction, the  $[\text{Mn}(\alpha\text{-diimine})(\text{CO})_3\text{L}]^n$  systems, where  $\text{L}$  is a neutral or anionic monodentate ligand such as acetonitrile ( $\text{CH}_3\text{CN}$ ;  $n = 1+$ ) or  $\text{Br}^-$  ( $n = 0$ ), are among the most highly studied.<sup>1,2</sup> This is in part due to the abundance and low-cost of manganese but also due to the capacity for these catalysts to exhibit a high turnover frequency (TOF),<sup>3,4</sup> and a tunable and high product selectivity with, on occasion, a high turnover number (TON).<sup>5,6</sup> The majority of these studies have utilized conventional 2,2'-bipyridyl (bpy)-based  $\alpha$ -diimine ligands, inspired no doubt by the early works of Hawecker, Lehn and Ziessel<sup>7,8</sup>, and Meyer<sup>9</sup> on  $[\text{ReCl}(\text{bpy})(\text{CO})_3]$ , as well as the more recent study by Chardon-Noblat, Deronzier and co-workers on  $[\text{MnBr}(\text{dmbpy})(\text{CO})_3]$  ( $\text{dmbpy} = 4,4'$ -dimethyl-2,2'-bipyridine).<sup>10</sup> In contrast to their  $\text{Re}(\text{I})$  analogues, apart from select examples,<sup>4,11-13</sup>  $\text{Mn}(\text{I})$ -based pre-catalysts typically require the presence of excess Brønsted acid for the binding of  $\text{CO}_2$  and formation of a key  $\text{Mn}(\text{I})$  metallocarboxylic acid intermediate.<sup>14,15</sup> An increasing number of these Mn-based catalysts now deviate from the traditional  $\alpha$ -diimine ligand framework, taking advantage of a variety of symmetric and asymmetric ligand scaffolds.<sup>1</sup>

For example, Agarwal and co-workers first employed this approach through the introduction of the asymmetric 2-pyridyl  $N$ -heterocyclic carbene (NHC) ligand in a manganese(I) tricarbonyl bromide pre-catalyst, later improved upon with the more  $\pi$ -acidic 2-pyrimidyl NHC ligand.<sup>16,17</sup> This work was followed by Hartl, Weinstein, and co-workers who developed a series of catalysts based upon the asymmetric 2-(phenylimino)pyridine ligand system where imine substituents were used to tune the redox properties of the  $\text{Mn}(\text{I})$  center while 2,6-phenyl substituents were used to introduce steric bulk.<sup>18</sup> More recently, Richeson and co-workers reported highly selective CO evolution by the  $[\text{mer-Mn}(\text{PNP})(\text{CO})_3]^+$  and  $[\text{fac-MnBr}(\text{PN})(\text{CO})_3]$  pre-catalysts, where PNP is the  $N,N$ -bis(diphenylphosphino)-2,6-di(methylamino)pyridine pincer ligand and PN is the bidentate  $N$ -(diphenylphosphino)-2-(methylamino)pyridine ligand.<sup>12</sup> Adopting a symmetric approach, Royo, Lloret-Fillol, and co-workers used a methylene bridged bidentate bis( $N$ -methylimidazolium) ligand which exhibited the highest  $\text{TOF}_{\text{max}}$  for any Mn-based electrocatalyst reported to date, albeit with an inherently high overpotential due to the electron-rich properties of the ligand.<sup>4</sup>

In this study, the asymmetric bidentate electron-rich 5,7-dimethyl-8-oxyquinolate ( $\text{Me}_2\text{OQN}^-$ ) ligand is investigated at both  $\text{Re}(\text{I})$  and  $\text{Mn}(\text{I})$  *facial*-tricarbonyl solvated

metal centers, and compared against the redox and electrocatalytic properties of their Re(I) and Mn(I) bpy counterparts for reference (Fig. 1).

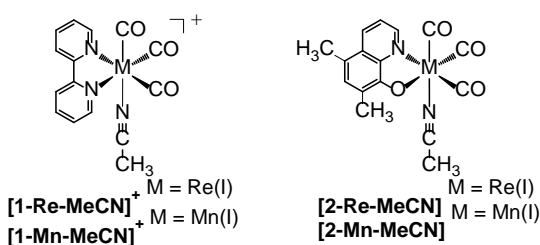


Figure 1. Molecular structures of  $[\text{M}(\text{bpy})(\text{CO})_3(\text{CH}_3\text{CN})]^+$  (**[1-M-MeCN]<sup>+</sup>**,  $\text{M} = \text{Re}(\text{I})$  or  $\text{Mn}(\text{I})$ ) and  $[\text{M}(\text{Me}_2\text{OQN})(\text{CO})_3(\text{CH}_3\text{CN})]$  (**[2-M-MeCN]**,  $\text{M} = \text{Re}(\text{I})$  or  $\text{Mn}(\text{I})$ ).

This design is inspired by the copper-based monoamine and galactose oxidase enzymes, where a tyrosine O-radical/anion redox couple works in synergy with the Cu(II/I) redox couple to promote two-electron two-proton coupled amine/alcohol oxidation and dioxygen reduction.<sup>19-22</sup> Indeed, metalloradicals and redox transformations are the cornerstone of most catalytic cycles with growing importance today being given to catalysts possessing so-called '*non-innocent*' ligands<sup>23, 24</sup> which may be directly involved in the redox transformations of the catalytic cycle.<sup>25-31</sup> In this study, using a suite of experimental and computational techniques, we test the hypothesis that a ligand-based radical/anion redox couple may participate synergistically with the Re(I/0) or Mn(I/0) couple to effect the two-electron two-proton coupled reduction of  $\text{CO}_2$  to CO. This demonstrates that both ligand and metal can share redox accountability, contributing one electron each towards catalyst activation, and ultimately CO evolution.

## RESULTS

### Synthesis and Structural Characterization

The syntheses of **[1-Re-MeCN]<sup>+</sup>**, **[1-Mn-MeCN]<sup>+</sup>**, and **[2-Re-MeCN]** were successfully completed following previously reported literature procedures.<sup>32-34</sup> Unlike in the previous report for **[2-Re-MeCN]**,<sup>33</sup> **[2-Mn-MeCN]** could not be isolated directly. Instead, the  $[\text{Mn}(\text{Me}_2\text{OQN})(\text{CO})_3(\text{THF})]$  complex was firstly prepared by deprotonating the commercially available 5,7-dimethyl-8-hydroxyquinoline ligand with a slight excess of potassium carbonate in dry tetrahydrofuran, followed by addition of bromopentacarbonyl manganese(I) and heating in a microwave reactor at 60 °C for 1 hour. Cooling to room temperature and recrystallization yielded analytically pure product. The  $[\text{Mn}(\text{Me}_2\text{OQN})(\text{CO})_3(\text{THF})]$  complex exhibits very similar solvation behavior to **[2-Re-MeCN]**, whereby in non-coordinating solvents the weakly bound monodentate THF ligand dissociates, forming the  $[\text{Mn}(\text{Me}_2\text{OQN})(\text{CO})_3]_2$  dimer as confirmed by FTIR spectroscopy in dichloromethane. Similar again to

**[2-Re-MeCN]**, immediate solvation of the dimer occurs in neat acetonitrile, quantitatively forming **[2-Mn-MeCN]** in-situ (Scheme 1), confirmed by FTIR (Fig. 2) and <sup>1</sup>H NMR (Fig. SI-1) spectroscopy.

**Scheme 1. Solvation of the  $[\text{M}(\text{Me}_2\text{OQN})(\text{CO})_3]_2$  dimer in acetonitrile, forming the acetonitrile solvated **[2-M-MeCN]** monomers ( $\text{M} = \text{Mn}$  or  $\text{Re}$ )**

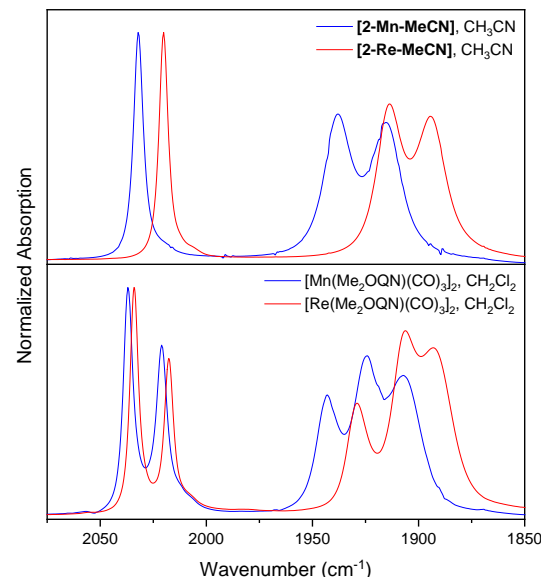
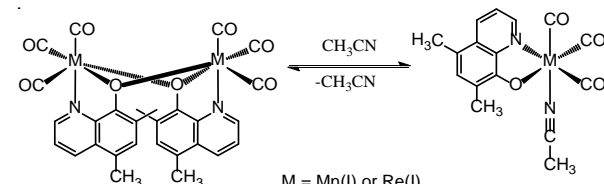


Figure 2. Overlay of FTIR spectra for **[2-Re-MeCN]** and **[2-Mn-MeCN]** recorded in acetonitrile (top), and the dimeric  $[\text{M}(\text{Me}_2\text{OQN})(\text{CO})_3]_2$  ( $\text{M} = \text{Mn}$  or  $\text{Re}$ ) complexes recorded in dichloromethane (bottom).

The FTIR spectra of both monomer and dimer Mn or Re complexes exhibit characteristic  $\nu(\text{CO})$  stretching modes in the 1850–2050 cm<sup>-1</sup> range. In non-coordinating dichloromethane, the  $[\text{M}(\text{Me}_2\text{OQN})(\text{CO})_3]_2$  ( $\text{M} = \text{Mn}$  or  $\text{Re}$ ) spectra are best described as symmetric and asymmetric combinations of both *fac*- $\text{M}(\text{CO})_3$  centers in the dimeric structure. The Mn dimer exhibits a symmetric and asymmetric combination of each tricarbonyl A(1)' stretching mode at 2037 and 2021 cm<sup>-1</sup>, while the equivalent Re dimer bands are shifted to slightly lower wavenumber, at 2034 and 2017 cm<sup>-1</sup>, consistent with the Re center being more electron rich. The three absorption bands observed for the  $[\text{Mn}(\text{Me}_2\text{OQN})(\text{CO})_3]_2$  dimer in dichloromethane at 1943, 1924 and 1907 cm<sup>-1</sup> are due to unresolved overlap of four  $\nu(\text{CO})$  stretches due to symmetric and asymmetric

coupling of each  $\text{Mn}(\text{CO})_3$  center  $\text{A}(2)'$  and  $\text{A}''$  stretching modes. Again, the Re dimer exhibits a similar profile but shifted to lower wavenumbers at 1929, 1906 and 1893  $\text{cm}^{-1}$ . In acetonitrile, both the **[2-Mn-MeCN]** and **[2-Re-MeCN]** monomers exhibit the more common three peak profile typically observed for *fac*-tricarbonyl metal complexes possessing pseudo- $C_3$  point group symmetry. **[2-Mn-MeCN]** exhibits  $\text{A}(1)'$ ,  $\text{A}(2)'$ , and  $\text{A}''$   $\nu(\text{CO})$  stretching modes at 2032, 1938 and 1915  $\text{cm}^{-1}$ , respectively. The analogous  $\nu(\text{CO})$  stretching modes for the more electron rich Re complex, **[2-Re-MeCN]**, are observed at lower energy due to greater Re  $d(\pi) \rightarrow \text{CO}(\pi^*)$  back-donation, with peaks at 2020, 1913 and 1894  $\text{cm}^{-1}$ .

### Electronic structure calculations and cyclic voltammetry under 1 atm of argon

Prior to electrocatalysis studies it is important to gain an in-depth understanding of pre-catalyst redox properties under inert conditions in the absence of  $\text{CO}_2$ . In this particular study it is also relevant to highlight the unique redox characteristics of Re and Mn tricarbonyl complexes with the non-innocent  $\text{Me}_2\text{OQN}^-$  ligand. In a previous study by Zhao et al.,<sup>33</sup> the ‘redox-active’ label for the bpy ligand was distinguished from the more complex ‘non-innocent ligand’<sup>35</sup> character of the  $\text{Me}_2\text{OQN}^-$  ligand in **[2-Re-MeCN]**, at least at its HOMO, HOMO-2 and HOMO-3 energy levels. Computational analysis predicts the HOMO level of **[1-Re-MeCN]<sup>+</sup>** to consist primarily of Re( $d$ ) and  $\text{CO}(\pi^*)$  character, with no contribution from the bpy ligand, whereas the non-innocent nature of the  $\text{Me}_2\text{OQN}^-$  ligand arises from degenerate mixing of the frontier Re  $d(\pi)$  and  $\text{Me}_2\text{OQN}^-$   $\pi$ -electron donating orbitals at the HOMO and HOMO-2 levels.<sup>33</sup> In the current study, to aid with electrochemical redox assignments, we investigated the net unpaired spin densities of the oxidized and reduced forms of **[2-Re-MeCN]** and **[2-Mn-MeCN]** as presented in Figure 3.

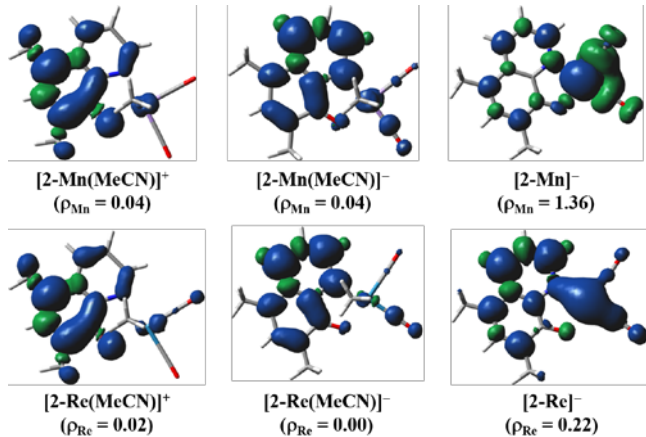


Figure 3. Spin density plots (isofactor = 0.001) computed at the M06 level of theory illustrating the significant contribution of the  $\text{Me}_2\text{OQN}^-$  ligand to the one-electron oxidized **[2-M-MeCN]<sup>+</sup>** complex, and the one-electron reduced six-coordinate **[2-M-MeCN]<sup>-</sup>** and five-coordinate **[2-M]<sup>-</sup>** complexes (M = Mn or Re).

One-electron oxidation of both **[2-Re-MeCN]** and **[2-Mn-MeCN]** leads to negligible net spin densities on the metal centers whereas significant spin is found to be delocalized on the phenolate ring of  $\text{Me}_2\text{OQN}^-$ , with  $\rho_{\text{O}} = 0.22\text{--}0.24$ . As a result, the oxidized species could be assigned as  $[\text{M}^{\text{I}}(\text{Me}_2\text{OQN}^*)(\text{MeCN})]^+$ . Similarly, one-electron reduction results in the reduction of the ligand, which could be viewed as  $[\text{M}^{\text{I}}(\text{Me}_2\text{OQN}^-)(\text{MeCN})]^-$ . However, this time higher spin density is localized on the pyridyl-side of the quinoline ring with  $\rho_{\text{N}} = 0.23$  and  $\rho_{\text{O}} = 0.01$ , indicating negligible radical character on the oxygen atom. Upon dissociation of the acetonitrile ligand, the unpaired spin localizes on the metal center for **[2-Mn]<sup>-</sup>** ( $\rho_{\text{Mn}} = 1.36$ ) whereas it is shared between the  $\text{Me}_2\text{OQN}^-$  ligand and the metal center for **[2-Re]<sup>-</sup>** ( $\rho_{\text{Re}} = 0.22$ ) (Fig. 3). The unpaired spin density data for both five-coordinate one-electron reduced **[1-Re]<sup>0</sup>** and **[1-Mn]<sup>0</sup>** complexes is similar to their counterparts with the  $\text{Me}_2\text{OQN}^-$  ligand, but an inspection of Mulliken charges indicates an increased electron density on each metal center in the latter as expected from the anionic nature of the  $\text{Me}_2\text{OQN}^-$  ligand (Fig. SI-18). The electrochemical redox potentials for both **[2-Re-MeCN]** and **[2-M-MeCN]** have been investigated by cyclic voltammetry and are presented below in Figure 4. For cyclic voltammetry plots directly comparing **[1-M-MeCN]<sup>+</sup>** and **[2-M-MeCN]<sup>+</sup>** (M = Mn or Re) complexes, the reader is referred to the supporting information (Figs. SI-3 and SI-4).

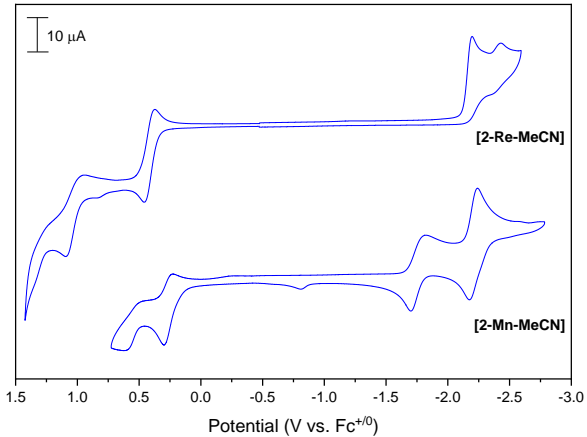


Figure 4. Cyclic voltammograms of **[2-Re-MeCN]** and **[2-Mn-MeCN]** recorded under 1 atm of argon with a 3 mm glassy carbon disc working electrode, and 1 mM analyte concentration in 0.1 M  $[\text{Bu}_4\text{N}]^+[\text{PF}_6]^-$  acetonitrile supporting electrolyte with a scan rate of 0.10 V s<sup>-1</sup>.

The voltammetry of Re bpy complexes is well established.<sup>9</sup> As shown in Fig. SI-3 for **[1-Re-MeCN]<sup>+</sup>**, a quasi-reversible one-electron oxidation event occurs at +1.49 V vs the ferricinium/ferrocene ( $\text{Fc}^{+/0}$ ) pseudo-reference redox couple (all potentials are hereafter reported vs  $\text{Fc}^{+/0}$ ). Due to the electron rich character of the  $\text{Me}_2\text{OQN}^-$  ligand in **[2-Re-MeCN]**, its first oxidation occurs at +0.40 V (Fig. 4), which is >1 V negative of the Re(II/I) couple in **[1-Re-MeCN]<sup>+</sup>**. Negligible Re(II) character is present in **[2-Re-**

**MeCN**]<sup>+</sup>. Furthermore, this primarily ligand-based **[2-Re-MeCN]**<sup>(+/-0)</sup> redox couple is reversible. It is only upon 2-electron oxidation at +1.00 V that the redox chemistry of **[2-Re-MeCN]**<sup>(2+/-)</sup> becomes quasi-reversible likely due to decreased Re  $d(\pi) \rightarrow \text{CO}(\pi^*)$  back-bonding and CO dissociation. The reductive chemistry of **[1-Re-MeCN]**<sup>+</sup> follows an electrochemical-electrochemical-chemical (ECE) mechanism, as described earlier by Sullivan et al.<sup>9</sup> Correlation of our own voltammetric data with computational analysis is consistent with this EEC mechanism. The bpy( $\pi^*$ )-based LUMO of **[1-Re-MeCN]**<sup>+</sup> is electronically independent of the Re(I) center. However, it is still redox-active and displays a quasi-reversible one-electron reduction at -1.61 V, followed by the Re(I/0) couple at -1.78 V (Fig. SI-3). This second reduction is irreversible due to dissociation of the monodentate acetonitrile ligand, forming the five coordinate, two-electron reduced  $[\text{Re}^0(\text{bpy}^*)(\text{CO})_3]^-$  species, which has previously been established as the active catalyst for  $\text{CO}_2$  reduction.<sup>14</sup> Upon switching the bpy ligand in cationic **[1-Re-MeCN]**<sup>+</sup> to the anionic  $\text{Me}_2\text{OQN}^-$  ligand in the neutral **[2-Re-MeCN]** complex, two irreversible one-electron reduction events are observed at -2.23 and -2.46 V (Fig. 4). As will be described below via computational and spectroelectrochemical EPR analysis, these are both assigned to the  $\text{Me}_2\text{OQN}^{(-/-)}$  redox couple according to an ECE mechanism. The first  $\text{Me}_2\text{OQN}^{(-/-)}$ -based reduction forms the anionic  $[\text{Re}^1(\text{Me}_2\text{OQN}^*)\text{(CO)}_3(\text{CH}_3\text{CN})]^-$  intermediate, which gives rise to dissociation of the monodentate acetonitrile ligand, facilitating a thermal migration of the added electron density onto the Re center to form the anionic five coordinate  $[\text{Re}^0(\text{Me}_2\text{OQN})(\text{CO})_3]^-$  intermediate, allowing for a second ligand-based reduction to generate  $[\text{Re}^0(\text{Me}_2\text{OQN}^*)\text{(CO)}_3]^{2-}$ .

The reductive chemistry of **[1-Mn-MeCN]**<sup>+</sup> is now also well established and follows an ECE mechanism.<sup>1</sup> The first reduction of **[1-Mn-MeCN]**<sup>+</sup> at -1.48 V is bpy( $\pi^*$ )-based (Fig. SI-4). This is followed by rapid dissociation of the monodentate  $\text{CH}_3\text{CN}$  ligand, forming the five-coordinate neutral  $[\text{Mn}^0(\text{bpy})(\text{CO})_3]$  metalloradical, which rapidly dimerizes to form  $[\text{Mn}^0(\text{bpy})(\text{CO})_3]_2$ . Subsequent reduction of this  $\text{Mn}^0-\text{Mn}^0$  dimer is observed at -1.83 V, giving rise to the two-electron reduced five coordinate  $[\text{Mn}^0(\text{bpy}^*)(\text{CO})_3]^-$  active catalyst. Notably, oxidation of the  $\text{Mn}^0-\text{Mn}^0$  dimer is observed at -0.61 V upon the reverse scan in cyclic voltammetry. The Mn-Me<sub>2</sub>OQN based complex, **[2-Mn-MeCN]** exhibits analogous electrochemical behavior to the **[2-Re-MeCN]** system, albeit with slightly more positive potentials. Two sequential one-electron reductions are observed for **[2-Mn-MeCN]** at -1.66 V and -2.21 V (Scheme 2, Figure 4). The first reduction at -1.66 V forms the five-coordinate  $[\text{Mn}^0(\text{Me}_2\text{OQN})(\text{CO})_3]^-$  anion, as predicted by computational analysis (Fig. 3) and also confirmed by EPR and PR-TRIR experiments (vide infra). The second reduction occurring at -2.21 V subsequently forms the  $[\text{Mn}^0(\text{Me}_2\text{OQN}^*)\text{(CO)}_3]^{2-}$  di-anion. In addition, a weak anodic peak is evident at -0.81 V. This is tentatively assigned to oxidation of the monoanionic  $[\text{Mn}^0(\text{Me}_2\text{OQN})(\text{CO})_3]^-$  dimer likely formed by displacement of the solvent ligand in **[2-Mn-MeCN]** by the  $[\text{Mn}^0(\text{Me}_2\text{OQN})(\text{CO})_3]$  metalloradical via  $\text{Mn}^1-\text{Mn}^0$

bond formation. This is discussed further below in the pulse-radiolysis TRIR section. A collection of all redox potentials is provided here in Table 1 for reference.

**Scheme 2. The electrochemical-chemical-electrochemical (ECE) mechanism exhibited by **[2-Mn-MeCN]** and **[2-Re-MeCN]** upon sequential two-electron reduction**

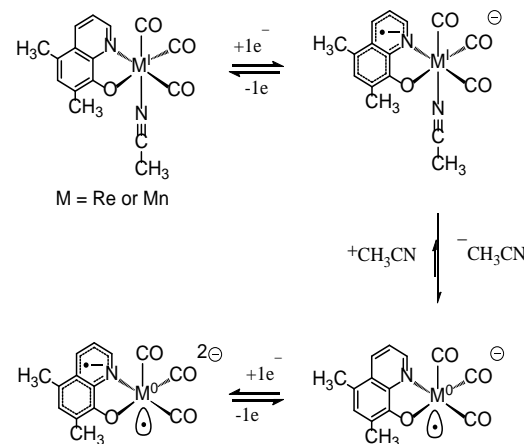


**Table 1. Electrochemical data recorded in 0.1 M  $[\text{Bu}_4\text{N}][\text{PF}_6]$  acetonitrile supporting electrolyte under 1 atm of argon at a glassy carbon working electrode with a scan rate of 0.10 V s<sup>-1</sup>**

$E$ (V vs. $\text{Fc}^{+/-}$ )					
$[\text{1-Re-MeCN}]^+$	+1.49 <sup>b</sup>	-1.65 <sup>b</sup>	-1.78 <sup>a</sup>	-2.94 <sup>a</sup>	
$[\text{2-Re-MeCN}]$	+1.00 <sup>b</sup>	+0.40 <sup>c</sup>	-2.23 <sup>a</sup>	-2.46 <sup>a</sup>	
$[\text{1-Mn-MeCN}]^+$	+1.03 <sup>a</sup>	-0.61 <sup>d</sup>	-1.48 <sup>a</sup>	-1.83 <sup>a</sup>	-2.94 <sup>b</sup>
$[\text{2-Mn-MeCN}]$	+0.62 <sup>a</sup>	+0.27 <sup>c</sup>	-0.81 <sup>d</sup>	-1.66 <sup>b</sup>	-2.21 <sup>c</sup>

<sup>a</sup> irreversible,  $E_{\text{pc}}$  or  $E_{\text{pa}}$  tabulated <sup>b</sup> quasi-reversible <sup>c</sup> reversible <sup>d</sup>  $E_{\text{pa}}$  associated with dimer oxidation

### Cyclic voltammetry under 1 atm of $\text{CO}_2$

Upon repeating cyclic voltammetry under 1 atm of  $\text{CO}_2$  (0.28 M) in acetonitrile with 0.17 M  $\text{H}_2\text{O}$  present, catalytic current is observed to grow in for **[1-Re-MeCN]**<sup>+</sup> at its second reduction wave, consistent with the well-established two-electron reduced species  $[\text{Re}^0(\text{bpy}^*)(\text{CO})_3]^-$  being the active catalyst.<sup>14</sup> It should be noted that under the current experimental conditions, with a low concentration of proton source, the initial catalytic current observed upon two-electron reduction is rather weak for **[1-Re-MeCN]**<sup>+</sup>. Increased catalytic current is observed upon scanning more negative to potentially higher reduced catalytic species. A significant improvement in the catalytic performance of **[1-Re-MeCN]**<sup>+</sup> is observed under more acidic conditions (Fig. SI-10). The five-coordinate anionic catalyst generated in-situ **[1-Re]**<sup>-</sup> can react with  $\text{CO}_2$  in the presence of a proton source, in this case

$\text{H}_2\text{O}$ , to generate the neutral  $[\text{Re}(\text{bpy})(\text{CO})_3(\text{CO}_2\text{H})]$  metallocarboxylic acid intermediate, which proceeds to evolve  $\text{H}_2\text{O}$  and  $\text{CO}$  upon further reduction.<sup>1, 15</sup> The full catalytic cycle for this reaction, and for the remaining catalysts in this study, is discussed in further detail below in the computational section; for the time being we will focus on the identity of each active catalyst generated in-situ. In contrast, and remarkably, **[2-Re-MeCN]** shows clear evidence for the onset of catalytic current upon the first one-electron reduction event when recorded under 1 atm of  $\text{CO}_2$  (Fig. 5,  $E_{\text{cat}/2} = -2.27$  V).

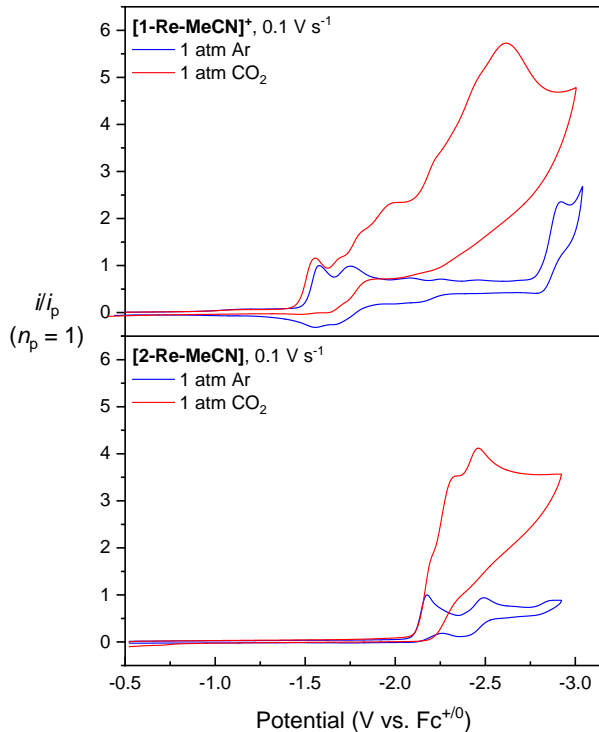


Figure 5. Cyclic voltammograms of **[1-Re-MeCN]<sup>+</sup>** (top) and **[2-Re-MeCN]** (bottom) recorded with 1 mM analyte concentration in 0.1 M  $[\text{Bu}_4\text{N}][\text{PF}_6]$  acetonitrile electrolyte with 0.17 M  $\text{H}_2\text{O}$ , under 1 atm of argon (blue) and 1 atm of  $\text{CO}_2$  (red) at a 3 mm glassy carbon disc working electrode with a scan rate of  $0.10 \text{ V s}^{-1}$ . Both sets of voltammograms are normalized with respect to the non-catalytic Faradaic current,  $i_p$ , observed at the peak of the first reduction wave under argon ( $n_p$  is the number of electrons involved in the non-catalytic Faradaic current response).

The magnitude of the catalytic current response exhibits first-order kinetic behavior with respect to the concentration of **[2-Re-MeCN]** (Fig. SI-5), providing support for our hypothesis that the  $\text{Me}_2\text{OQN}^{(\bullet/-)}$  redox couple is working in synergy with the  $\text{Re}(\text{I}/\text{O})$  couple to initiate formation of the key  $[\text{Re}^{\text{I}}(\text{Me}_2\text{OQN}^{\bullet})(\text{CO})_3(\text{CO}_2\text{H})]$  intermediate along the  $\text{CO}_2$  reduction catalytic cycle. Although the coulombic impact of the negatively charged  $\text{Me}_2\text{OQN}^-$  ligand requires a more negative potential to form the one-electron reduced derivative relative to **[1-Re-MeCN]<sup>+</sup>**, the **[2-Re-MeCN]** pre-catalyst exhibits a sharper growth

of catalytic current likely due to its inherently greater nucleophilicity. It is also noteworthy that a second peak is exhibited at  $-2.46$  V under catalytic conditions likely due to a parallel catalytic cycle stemming from the two-electron reduced **[2-Re]<sup>2-</sup>** active catalyst.

Recent evidence has shown that, while Mn-based catalysts can also bind  $\text{CO}_2$ , due to the lesser nucleophilicity of Mn vs Re they typically require a larger overpotential than their Re counterparts to drive catalytic  $\text{CO}$  formation at a similar rate to Re.<sup>1, 15</sup> This is due to the relatively lower energy of first-row vs. third-row valence *d*-orbitals.<sup>14</sup> The electrocatalytic properties of **[1-Mn-MeCN]<sup>+</sup>** have already been discussed at great length elsewhere.<sup>1</sup> In the context of this study, it is important to appreciate that following two-electron reduction to form the five-coordinate  $[\text{Mn}^0(\text{bpy})^{\bullet}(\text{CO})_3]^-$  active catalyst, a large overpotential is observed due to the required reduction of the  $[\text{Mn}(\text{bpy})(\text{CO})_3(\text{CO}_2\text{H})]$  intermediate in order to provide enough driving force for the rate-determining, proton-mediated C–OH bond cleavage step.<sup>1</sup> The need for this additional reduction step to promote rate-determining C–OH bond cleavage is characteristic of most Mn-based catalysts and is commonly referred to as the *reduction-first* catalytic pathway.<sup>1, 15</sup> In contrast to **[1-Mn-MeCN]<sup>+</sup>**, pre-catalyst **[2-Mn-MeCN]** exhibits onset for catalytic current directly upon formation of the two-electron reduced  $[\text{Mn}(\text{Me}_2\text{OQN})(\text{CO})_3]^{2-}$  intermediate (Fig. 6), thus avoiding any excessive overpotential beyond in-situ generation of the active catalyst ( $E_{\text{cat}/2} = -2.14$  V). This is consistent with pre-catalyst **[2-Mn-MeCN]** undergoing the proton-mediated C–OH bond cleavage step immediately upon two-electron reduction. In fact there is a significant anodic shift of the catalytic wave ( $E_{\text{cat}/2} = -2.14$  V) relative to the second-cathodic wave observed under inert conditions ( $E = -2.25$  V), which might be due to the binding of  $\text{CO}_2$  (Fig. 6).

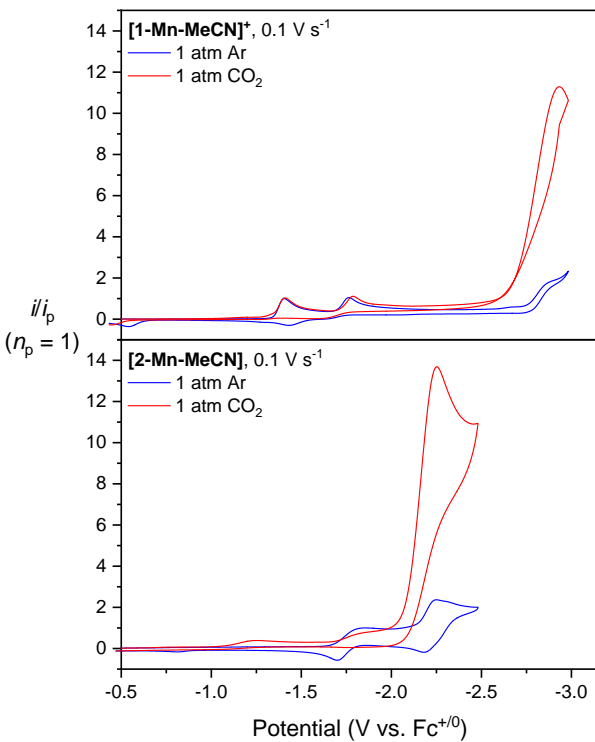


Figure 6. Cyclic voltammograms of **[1-Mn-MeCN]<sup>+</sup>** (top) and **[2-Mn-MeCN]** (bottom) recorded with 1 mM analyte concentration in 0.1 M  $[\text{Bu}_4\text{N}][\text{PF}_6]$  acetonitrile + 0.17 M  $\text{H}_2\text{O}$  electrolyte, under 1 atm of argon (blue) and 1 atm of  $\text{CO}_2$  (red) at a 3 mm glassy carbon disc working electrode with a scan rate of  $0.10 \text{ V s}^{-1}$ . Both sets of voltammograms are normalized with respect to the non-catalytic Faradaic current,  $i_p$ , observed at the peak of the first reduction wave under argon ( $n_p$  is the number of electrons involved in the non-catalytic Faradaic current response).

To summarize, in comparison to **[1-Re-MeCN]<sup>+</sup>** and **[1-Mn-MeCN]<sup>+</sup>**, the  $\text{Me}_2\text{OQN}^-$  based pre-catalysts exhibit onset of catalytic current with the input of one less equivalent of electrons to access the rate-determining  $\text{C}-\text{OH}$  bond cleavage step. Furthermore, both **[2-Re-MeCN]** and **[2-Mn-MeCN]** exhibit first-order kinetics with respect to both catalyst and  $\text{CO}_2$  concentration (Figs. SI-5 through SI-8). At least for the **[2-Re-MeCN]** pre-catalyst, this behavior is attributed to the formal  $\text{Me}_2\text{OQN}^{(\cdot/-)}$  redox couple which contributes in tandem with the  $\text{Re(I/O)}$  redox couple to  $\text{CO}_2/\text{H}^+$  activation (see computational section below for more details). In contrast to **[2-Re-MeCN]**, the **[2-Mn-MeCN]** pre-catalyst still requires two-electron reduction to access the metallocarboxylic acid intermediate. Direct onset of catalytic current from the two-electron reduced pentacoordinate species **[2-Mn]<sup>2-</sup>** is likely the consequence of a beneficial coulombic effect allowing for direct protonation to access the protonation mediated rate-determining  $\text{C}-\text{OH}$  bond cleavage step. In contrast, the bpy-based pre-catalyst **[1-Mn-MeCN]<sup>+</sup>** is converted to the pentacoordinate **[1-Mn]<sup>-</sup>** active catalyst in-situ, but upon  $\text{CO}_2/\text{H}^+$  binding to form the **[1-Mn-CO<sub>2</sub>H]** intermediate a further reduction event, and inherent overpotential, is required to form the

anionic **[Mn-CO<sub>2</sub>H]<sup>-</sup>** intermediate to access the rate-determining step via the so-called *reduction-first* catalytic pathway.<sup>1,15</sup>

A comparison of scan-rate dependent catalytic ( $i_{\text{cat}}$ ) and non-catalytic ( $i_p$ ) current ratio, i.e. scan-rate dependence of  $i_{\text{cat}}/i_p$ , allows for the identification of steady-state kinetic conditions and estimation of the maximum obtainable turnover frequency ( $\text{TOF}_{\text{max}}$ ) for a well-behaved catalyst according to eq. 1,

$$\text{TOF} = 0.1992 \left( \frac{Fv}{RT} \right) \left( \frac{n_p^3}{n_{\text{cat}}^2} \right) \left( \frac{i_{\text{cat}}}{i_p} \right)^2 \quad (1)$$

where  $F$  is the Faraday constant ( $96,485 \text{ s A mol}^{-1}$ ),  $v$  is the scan rate ( $\text{V s}^{-1}$ ),  $R$  is the universal gas constant ( $8.3145 \text{ V A s K}^{-1} \text{ mol}^{-1}$ ),  $T$  is the temperature ( $K$ ),  $n_p$  is the number of electrons involved in the non-catalytic Faradaic current response (responsible for  $i_p$ ), and  $n_{\text{cat}}$  is the number of electrons required for catalysis (2 electrons for the reduction of  $\text{CO}_2$  to  $\text{CO}$ ). A plot of  $\text{TOF}$  vs scan rate for both **[2-Re-MeCN]** and **[2-Mn-MeCN]** is presented in Figure 7.

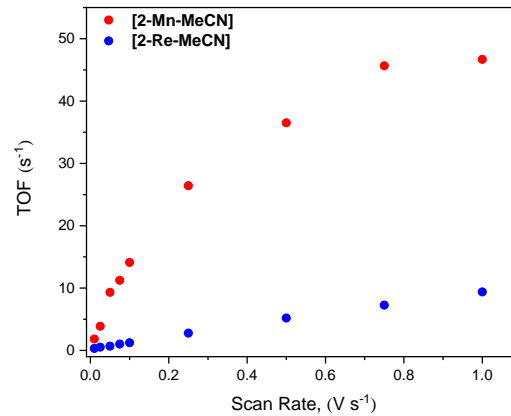


Figure 7. Scan-rate dependence of the turnover frequency (TOF) observed for **[2-Re-MeCN]** and **[2-Mn-MeCN]** recorded in 0.1 M  $[\text{Bu}_4\text{N}][\text{PF}_6]$  acetonitrile electrolyte with 0.17 M  $\text{H}_2\text{O}$  under 1 atm of  $\text{CO}_2$ . Steady-state kinetic conditions for **[2-Mn-MeCN]** are identified above a threshold scan rate of  $v \geq 0.75 \text{ V s}^{-1}$  by a plateau of the TOF response.

Steady-state conditions are established for **[2-Mn-MeCN]** at  $v \geq 0.75 \text{ V s}^{-1}$ , resulting in an estimated  $\text{TOF}_{\text{max}}$  value of  $45.4 \pm 8.4 \text{ s}^{-1}$ . Unfortunately, steady-state conditions could not be verified for pre-catalysts **[1-Re-MeCN]<sup>+</sup>**, **[1-Mn-MeCN]<sup>+</sup>** and **[2-Re-MeCN]**, as upon increasing the scan-rate their TOFs continued with a linear progression with no signs of a plateau current (Fig. SI-9). While this may be construed (incorrectly) as a consequence of rapid catalyst turnover, the inherently low  $i_{\text{cat}}/i_p$  ratios suggest this is a consequence of catalyst inhibition by an unknown side-reaction and not rate-limiting  $\text{CO}_2$  substrate consumption. Attempts to estimate  $\text{TOF}_{\text{max}}$  using Saveant's foot-of-the-wave analysis (FOWA) method

were unsuccessful due to the weak catalytic currents observed and the limited linear portion of the sigmoidal current response.<sup>36, 37</sup> As such, the best-case alternative was to compare the  $i_{\text{cat}}/i_p$  ratios and non-optimized TOF values at a single scan rate of  $v = 0.10 \text{ V s}^{-1}$  (Table 2).

**Table 2. Summary of catalytic results for all complexes investigated. Results obtained from CV data recorded for 1 mM [catalyst] under 1 atm of CO<sub>2</sub> at 0.10 V s<sup>-1</sup>**

	$E_{\text{cat/2}}^a$	$i_{\text{cat}}/i_p$	TOF (s <sup>-1</sup> ) <sup>b</sup>
[1-Re-MeCN] <sup>+</sup>	-1.75 <sup>c</sup>	3.6	2.6
[2-Re-MeCN]	-2.27	2.5	1.2
[1-Mn-MeCN] <sup>+</sup>	-2.86	10.7	22.2
[2-Mn-MeCN]	-2.14	8.5	14.1

<sup>a</sup>Potentials reported as V vs. Fc<sup>+/-</sup>. <sup>b</sup>TOF values estimated from the ratio  $i_{\text{cat}}/i_p$  determined at  $v = 1.0 \text{ V s}^{-1}$  using eq. 1. <sup>c</sup> determined from the peak catalytic current at  $E_{\text{cat}} = -2.09 \text{ V}$ .

Notably, the **[1-Mn-MeCN]<sup>+</sup>** pre-catalyst exhibits the greatest TOF at 0.10 V s<sup>-1</sup> in the presence of 1 atm of CO<sub>2</sub> and 0.17 M H<sub>2</sub>O of 22.2 s<sup>-1</sup>. This comes at the cost of the most negative  $E_{\text{cat/2}}$  of -2.78 V. The **[2-Mn-MeCN]** catalyst exhibits a more favorable  $E_{\text{cat/2}}$  of -2.15 V albeit with a slightly lower TOF of 14.1 s<sup>-1</sup> under identical (non-steady state) experimental conditions. Both **[1-Re-MeCN]<sup>+</sup>** and **[2-Re-MeCN]** pre-catalysts exhibit smaller TOFs at just 2.6 s<sup>-1</sup> and 1.2 s<sup>-1</sup>, respectively. Cyclic voltammetry for all complexes was also conducted with 1 atm CO<sub>2</sub> under more acidic conditions, i.e., in the presence of 1.0 M trifluoroethanol (TFE). While the bpy-based pre-catalysts, **[1-Re-MeCN]<sup>+</sup>** and **[2-Re-MeCN]<sup>+</sup>** showed improved catalytic current under these conditions, the Me<sub>2</sub>OQN<sup>-</sup>-based catalysts exhibited a decreased catalytic current (Figs. SI-10 and SI-11), and also a decrease in selectivity for CO<sub>2</sub> reduction, confirmed by controlled potential electrolysis, as discussed below.

### Controlled potential electrolysis

To confirm the product selectivity of pre-catalysts **[1-Re-MeCN]<sup>+</sup>**, **[2-Re-MeCN]**, **[1-Mn-MeCN]<sup>+</sup>** and **[2-Mn-MeCN]**, controlled potential electrolysis (CPE) experiments with quantitative in-situ gas chromatography analysis were run for CO and H<sub>2</sub> quantification followed by a single solution phase analysis of the electrolyte solution for formate quantification post-catalysis, using ion-exchange chromatography. In CPE experiments, each catalyst was reduced at a single potential bias identified by cyclic voltammetry (typically at  $E_{\text{cat/2}}$ ) under 1 atm of CO<sub>2</sub> with 0.17 M H<sub>2</sub>O. All four catalysts exhibit formation of CO, albeit with varying efficiencies, with negligible observation of H<sub>2</sub> and/or formate. Pre-catalyst **[1-Re-MeCN]<sup>+</sup>** exhibits a moderate Faradaic efficiency of 52% for CO. The Mn-based bpy analogue, **[1-Mn-MeCN]<sup>+</sup>** exhibits similar behavior with 62% Faradaic efficiency for CO and just a 2% Faradaic efficiency for H<sub>2</sub>. The Me<sub>2</sub>OQN<sup>-</sup>-based pre-catalyst, **[2-Re-MeCN]** presents a similarly moderate Faradaic efficiency for CO production relative to **[1-Re-MeCN]<sup>+</sup>**, of 51%, with negligible H<sub>2</sub> at just 3%. However, pre-catalyst **[2-Mn-MeCN]**, exhibits much improved CO evolution, with a Faradaic efficiency of 88%.

**Table 3. Summary of Faradaic efficiencies achieved for each catalyst studied following 3 hours of controlled potential electrolysis at a potential determined by  $E_{\text{cat/2}}$  in the presence of 1 atm CO<sub>2</sub> and 0.17 M H<sub>2</sub>O**

	CO (%) <sup>a</sup>	H <sub>2</sub> (%) <sup>a</sup>	HCO <sub>2</sub> H (%) <sup>b</sup>
[1-Re-MeCN] <sup>+</sup>	52	0	0
[2-Re-MeCN]	51	3	0
[1-Mn-MeCN] <sup>+</sup>	62	2	0
[2-Mn-MeCN]	88	5	0

<sup>a</sup>Determined by GC chromatography, <sup>b</sup>Determined by ion-exchange chromatography

Attempts to account for missing Faradaic yield was unsuccessful. However, similar CPE experiments repeated in the presence of a larger excess of Brønsted acid, for example, 2.78 M (5%) H<sub>2</sub>O, allowed for quantitative assignment of the Faradaic yield, albeit with a much reduced selectivity for CO<sub>2</sub> reduction and increased H<sub>2</sub> yield. These data are summarized in Table SI-1.

### Electron Paramagnetic Resonance Spectroscopy

Electron paramagnetic resonance (EPR) is a valuable, structurally sensitive technique to gain insight into the mechanistic steps for electrocatalysis pertaining to paramagnetic redox intermediates of transition metal catalysts. Furthermore, both naturally occurring isotopes of rhenium, <sup>185</sup>Re (37.1% abundance) and <sup>187</sup>Re (62.9% abundance), as well as the sole <sup>55</sup>Mn isotope (100% abundance), each possess a nuclear spin angular momentum of  $I = 5/2$  giving rise to distinct hyperfine spectral features. EPR spectroscopy has already been employed in select studies to identify the nature of radical intermediates in the reduction of CO<sub>2</sub> using  $[\text{M}(\alpha\text{-diimine})(\text{CO})_3\text{L}]^n$ , M = Mn or Re, based pre-catalysts. For example, Kubiak and coworkers recently used EPR to confirm the ligand-based radical in a  $[\text{Re}(\text{MesDAB}^{\text{Me}+})]$  catalyst.<sup>29</sup> Kaim and coworkers have also used EPR extensively to study reduced states for a series of  $[\text{Re}(\text{bpy})(\text{CO})_3\text{L}]^n$  pre-catalysts.<sup>32</sup> A comparable EPR response is here observed for **[1-Re-MeCN]<sup>+</sup>** following one-electron reduction (Fig. SI-12) where computation predicts the spin density to be predominantly based in a bpy( $\pi^*$ ) orbital (Fig. SI-18). In contrast to **[1-Re-MeCN]<sup>+</sup>**, the Re center in **[2-Re-MeCN]** demonstrates notably different behavior after one-electron reduction (Fig. 8).

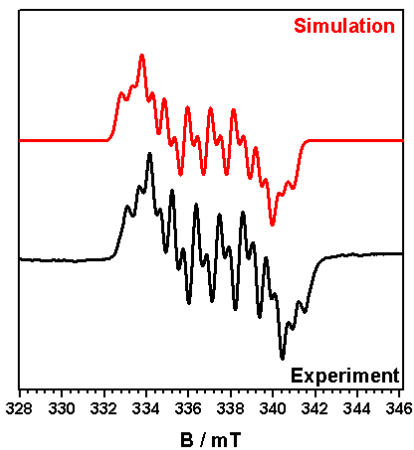


Figure 8. Experimental (X-band, 9.5 GHz,  $g = 2.004$ ) and simulated EPR spectroelectrochemical data for **[2-Re-MeCN]** recorded at 77 K in 0.1 M  $[\text{Bu}_4\text{N}][\text{PF}_6]$  acetonitrile electrolyte following one-electron reduction.

Clear evidence for an equilibrium mixture of two species is observed, consistent with the theoretical prediction for reversible dissociation of the acetonitrile solvent for the one-electron reduced species, i.e.  $[\text{2-Re-MeCN}]^- \rightleftharpoons [\text{2-Re}]^- + \text{MeCN}$ , to generate the pentacoordinate  $[\text{Re}^0(\text{Me}_2\text{OQN})(\text{CO})_3]^-$  metalloradical complex. Calculations suggest that the Re center is responsible for 22% of the spin character in  $[\text{2-Re}]^-$  (Fig. 3). This EPR spectrum is highly significant as it provides clear experimental evidence of the latter metalloradical species which is believed to be the active catalyst for  $\text{CO}_2$  reduction.

A broad EPR signal is observed upon one-electron reduction of **[1-Mn-MeCN]<sup>+</sup>**, which is solely attributed to the hexacoordinate  $[\text{Mn}^1(\text{bpy}^{\cdot-})(\text{CO})_3(\text{CH}_3\text{CN})]^0$  radical anion possessing a predominantly ligand-based radical ( $\rho_{\text{Mn}} = 0.00$ , Fig. SI-18). Again, hyperfine splitting is observed as a sextet consistent with coupling to the adjacent  $\text{Mn}^0$  ( $I = 5/2$ ) center (Fig. SI-13). It should be emphasized here that one-electron reduction of **[1-Mn-MeCN]<sup>+</sup>** leads to rapid formation of the EPR silent  $[\text{Mn}(\text{bpy})(\text{CO})_3]_2$  dimer. However, EPR is a very sensitive technique and is capable of characterizing even trace quantities of  $[\text{Mn}(\text{bpy})(\text{CO})_3(\text{CH}_3\text{CN})]^0$ .

In contrast, the strong sextet EPR signal exhibited upon one-electron reduction of **[2-Mn-MeCN]** (Fig. 9) provides strong evidence for the pure  $\text{Mn}(0)$  based pentacoordinate metalloradical species  $[\text{Mn}^0(\text{Me}_2\text{OQN})(\text{CO})_3]^-$ . The lack of additional hyperfine splitting here suggests that there is limited interaction of the unpaired electron with surrounding nuclei on the ligand, concluding that the radical is entirely based on the Mn center. This observation is also consistent with computational studies, which predict a spin-density of  $\rho_{\text{Mn}} = 1.36$  for  $[\text{Mn}^0(\text{Me}_2\text{OQN})(\text{CO})_3]^-$  (Fig. 3).

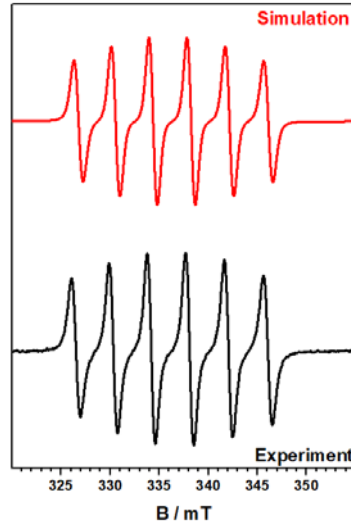


Figure 9. Experimental (X-band, 9.5 GHz) and simulated EPR spectroelectrochemical data for **[2-Mn-MeCN]** recorded at 77 K in 0.1 M  $[\text{Bu}_4\text{N}][\text{PF}_6]$  acetonitrile electrolyte following one-electron reduction ( $g = 2.007$ ).

### Pulse Radiolysis Time-Resolved Infrared Spectroscopy

In pulse radiolysis (PR), a high-energy electron pulse from an accelerator is used to excite a sample.<sup>38</sup> This rapidly generates a homogeneous mixture of reducing and oxidizing radicals derived from the solvent, which include the strongly reducing solvated electron ( $e_{\text{s}}^-$ ). Typically, an additive is used to scavenge undesired radicals and/or to convert the primary radicals into one type of radical species, thus creating either oxidizing or reducing conditions.<sup>38</sup> For the experiments discussed here in  $\text{CH}_3\text{CN}$ , formate ion ( $\text{OC}(\text{O})\text{H}^-$ ) was added to the solution as a radical scavenger. The H-atom transfer processes that it undergoes with the solvent radicals rapidly generate the strongly reducing carbon dioxide radical anion ( $\text{CO}_2^{\cdot-}$ ),<sup>39</sup> which, in addition to  $e_{\text{s}}^-$ , acts as a reductant towards the dissolved metal complex.

Combining PR with nanosecond time-resolved infrared (TRIR) detection has provided a powerful tool for mechanistic studies of electrocatalysts since specific redox intermediates can be rapidly prepared and identified, and their reactivity subsequently monitored.<sup>1, 40, 41</sup> Indeed, PR-TRIR has the time resolution to allow the detection of short-lived intermediates that cannot be observed by infrared spectroelectrochemistry (IR-SEC). For example, previous PR-TRIR studies of the mononuclear  $[\text{Mn}(\text{dtbpy})(\text{CO})_3(\text{OC}(\text{O})\text{H})]$  pre-catalyst in  $\text{CH}_3\text{CN}$ <sup>40</sup> allowed the observation of formate dissociation from the one-electron reduced  $[\text{Mn}(\text{dtbpy}^{\cdot-})(\text{CO})_3(\text{OC}(\text{O})\text{H})]^-$  transient ( $\tau = 77$  ns) with concomitant production of the neutral five-coordinate  $[\text{Mn}^0(\text{dtbpy})(\text{CO})_3]$  radical, and dimerization of this radical to form the Mn–Mn bound  $[\text{Mn}^0(\text{dtbpy})(\text{CO})_3]_2$  dimer. In contrast, PR-TRIR has also been used to demonstrate the absence of dimerization upon one-electron reduction of pre-catalysts that generate the bulky  $[\text{Mn}^0(\text{mes}_2\text{bpy})(\text{CO})_3]$  and  $\{\text{Mn}^0$

$\{[(\text{MeO})_2\text{Ph}]_{2\text{bpy}}(\text{CO})_3\}$  intermediates.<sup>3</sup> In these cases, the two-electron reduced species was observed to grow-in on the microsecond timescale, consistent with disproportionation of the one-electron reduced intermediate,<sup>3</sup> as previously implied by CV and IR-SEC experiments.<sup>42, 43</sup>

Upon preparation of solutions of **[2-Re-MeCN]** and **[2-Mn-MeCN]** for PR-TRIR experiments in  $\text{CH}_3\text{CN}$  in the presence of 50 mM  $[\text{Bu}_4\text{N}][\text{OC(O)H}]$  as a solvent radical scavenger, the large excess of formate ions quantitatively generated the **[2-Re-OC(O)H]<sup>-</sup>** and **[2-Mn-OC(O)H]<sup>-</sup>** anions in-situ, due to the strong coordinating nature of formate compared with  $\text{CH}_3\text{CN}$ . However, these complexes still contain the  $\text{Me}_2\text{OQN}^-$  ligand and metal centers in the M(I) oxidation state, thus allowing interpretation of any catalytic intermediates upon formate dissociation, since Mn-formate complexes have previously been shown to rapidly eject the formate ligand upon one-electron reduction.<sup>3, 40</sup> **[2-Re-OC(O)H]<sup>-</sup>** exhibits three  $\nu(\text{CO})$  bands at 2003, 1885 and 1866  $\text{cm}^{-1}$  in  $\text{CH}_3\text{CN}$  (Fig. 10, bottom). Upon one-electron reduction by PR, these peaks are bleached, giving immediate rise to two new  $\nu(\text{CO})$  stretching modes at 1975 and 1843(br)  $\text{cm}^{-1}$  (Fig. 10, top). By comparison with computed IR spectra of all reasonable intermediates at the M06 level of theory (Fig. SI-14), we assign these bands to the one-electron reduced, coordinatively unsaturated  $[\text{Re}^0(\text{Me}_2\text{OQN})(\text{CO})_3]^-$  anion produced upon formate dissociation, which is expected<sup>40</sup> to be extremely rapid (nanosecond timescale). Within 2  $\mu\text{s}$ , another band grows-in at 1997  $\text{cm}^{-1}$ . Again by comparison with computed IR spectra (Fig. SI-14), this is attributed to the A(1)'  $\nu(\text{CO})$  stretch of the hexacoordinate  $[\text{Re}(\text{Me}_2\text{OQN}^-)(\text{CO})_3(\text{CH}_3\text{CN})]^-$  solvated anion, with both its A(2)' and A''  $\nu(\text{CO})$  stretches obscured by the strong doublet bleach of the formate starting material. The latter is evident by a positive valley in the bleach signal at 1875  $\text{cm}^{-1}$  (Fig. 10).

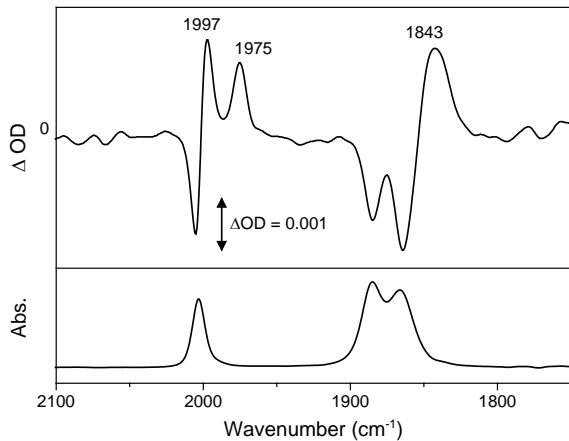


Figure 10. IR spectrum of a 1.5 mM solution of **[2-Re-OC(O)H]<sup>-</sup>** in  $\text{CH}_3\text{CN}$  containing 50 mM  $[\text{nBu}_4\text{N}][\text{OC(O)H}]$  (bottom) and the TRIR spectrum recorded 2  $\mu\text{s}$  after pulse radiolysis of this argon-purged solution (top).

The abovementioned PR-TRIR observations are consistent with the EPR and computational analysis of **[2-**

**Re-MeCN]** with respect to equilibria between the penta-coordinate  $[\text{Re}^0(\text{Me}_2\text{OQN})(\text{CO})_3]^-$  metalloradical and the hexacoordinate  $[\text{Re}(\text{Me}_2\text{OQN}^-)(\text{CO})_3(\text{CH}_3\text{CN})]^-$  solvated anion. These species were found to decay at different rates on the microsecond timescale, with the latter being more unstable. This is not surprising, since it was previously shown that formate ion only scavenges 60  $\pm$  20% of the radiolytic solvent radicals in  $\text{CH}_3\text{CN}$ ,<sup>39</sup> and thus the remaining radicals are likely to react with these two species at different rates due to their distinct radical characters. Since the actual decay pathways are unknown in the PR experiment, we will not discuss them further here.

**[2-Mn-OC(O)H]<sup>-</sup>** exhibits three  $\nu(\text{CO})$  stretches at 2013, 1909 and 1887  $\text{cm}^{-1}$  in  $\text{CH}_3\text{CN}$  (Fig. 11, bottom). All three are instantly bleached upon one-electron reduction by PR, giving immediate rise to a pair of sharp and broad  $\nu(\text{CO})$  bands at 1928 and 1810  $\text{cm}^{-1}$ , respectively (Fig. 11, top). The latter peaks are consistent with IR-SEC experiments (Fig. SI-15) upon one-electron reduction of **[2-Mn-MeCN]**, and are assigned to the five-coordinate  $[\text{Mn}^0(\text{Me}_2\text{OQN})(\text{CO})_3]^-$  metalloradical by comparison with the computed IR spectrum of this species (Fig. SI-16). Sole observation of the one-electron reduced  $[\text{Mn}^0(\text{Me}_2\text{OQN})(\text{CO})_3]^-$  metalloradical is also consistent with EPR and computational analysis of **[2-Mn-MeCN]**, and this species is found to decay slowly on the few hundred microseconds timescale, similar to the Re analog. Interestingly, there is also tentative evidence for a weak band at 2032  $\text{cm}^{-1}$  in the PR-TRIR spectrum (Fig. 11), which may correspond to a possible  $[\text{Mn}(\text{Me}_2\text{OQN})(\text{CO})_3]_2^-$  dimer, also observed by infrared spectroelectrochemistry (IR-SEC) at 1866(br), 1877 and 2032  $\text{cm}^{-1}$  (Figs. SI-13 & SI-15). Such dimer formation, albeit minor, may also be responsible for the weak oxidation wave observed at  $-0.81$  V by cyclic voltammetry (Fig. 4, Table 1).

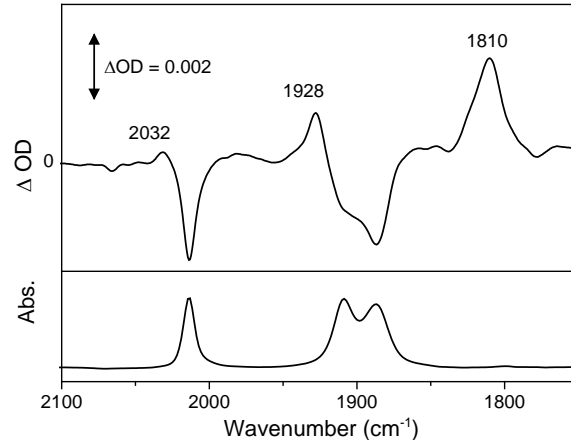


Figure 11. IR spectrum of a 1.5 mM solution of **[2-Mn-OC(O)H]<sup>-</sup>** in  $\text{CH}_3\text{CN}$  containing 50 mM  $[\text{nBu}_4\text{N}][\text{OC(O)H}]$  (bottom) and the TRIR spectrum recorded 15  $\mu\text{s}$  after pulse radiolysis of this argon-purged solution (top).

### Computational analysis

We performed density functional theory calculations at the M06-L and M06 level of theories coupled with the SMD continuum solvation model for acetonitrile (see computational methods for further details) to investigate the mechanism for proton-coupled electrocatalytic  $\text{CO}_2$  reduction catalyzed by both **[2-Re-MeCN]** and **[2-Mn-MeCN]**, including the electronic structures of catalytic intermediates, to produce CO and  $\text{H}_2\text{O}$ . The proposed catalytic cycle is presented in Scheme 3 including the computed standard reduction potentials ( $E^\circ$ ), free energy changes ( $\Delta G$ ) and activation free energies ( $\Delta G^\ddagger$ ). Plots of molecular orbitals and spin densities, are provided in the supporting information alongside the optimized transition-state structures for C–OH bond cleavage (Fig. SI-19). Here, the computed energetics at the M06 level of theory are presented with comparable data at the M06-L level of theory also available in supporting information. The proposed mechanism starts with a one-electron reduction step with concomitant dissociation of the acetonitrile ligand and leading to the formation of **[2-M]<sup>–</sup>** for both **[2-Mn-MeCN]** and **[2-Re-MeCN]** with computed  $E^\circ$  of –1.68 V and –2.25 V vs  $\text{Fc}^{+/0}$ , respectively, in quite good agreement with cyclic voltammetry experiments. The computed  $\Delta G$ s indicate that acetonitrile dissociation is irreversible for **[2-Mn]<sup>–</sup>** ( $\Delta G = –18.7$  kcal/mol) whereas it's possible to have an equilibrium in the case of **[2-Re]<sup>–</sup>** ( $\Delta G = –1.4$  kcal/mol). This is consistent with spectroelectrochemical EPR and PR-TRIR experiments. Acetonitrile dissociation upon one-electron reduction is also favorable for **[1-Mn-MeCN]<sup>+</sup>** ( $\Delta G = –6.6$  kcal/mol) but is unfavorable for **[1-Re-MeCN]<sup>+</sup>** ( $\Delta G = 4.1$  kcal/mol), also consistent with our experimental observations. As discussed above, in the resulting pentacoordinate species the spin is mostly localized on the metal center for **[2-Mn]<sup>–</sup>** ( $\rho_{\text{Mn}} = 1.36$ ) whereas it is delocalized across both the ligand and the metal center for **[2-Re]<sup>–</sup>** ( $\rho_{\text{Re}} = 0.22$ ).

Following the first reduction,  $\text{CO}_2$  binding to **[2-Re]<sup>–</sup>** ( $\Delta G = 12.6$  kcal/mol) is possible whereas we could not locate a  $\text{CO}_2$  bound adduct for the **[2-Mn]<sup>–</sup>** species, which is in line with the observed increase in catalytic current only for **[2-Re-MeCN]** at its first reduction potential (Fig. 5). Following  $\text{CO}_2$  binding and protonation ( $\Delta G = –11.2$  kcal/mol at pH 0) the neutral **[2-Re-CO<sub>2</sub>H]** metal-carboxylic intermediate of formula  $[\text{Re}^{\text{I}}(\text{Me}_2\text{OQN}^{\text{–}})(\text{CO})_3(\text{CO}_2\text{H})]$  is generated. Formation of the latter species is key to the unique electrocatalytic behavior exhibited by the **[2-Re-MeCN]** pre-catalyst. Consistent with a redox contribution from the  $\text{Me}_2\text{OQN}^{\text{–}}$  ligand towards  $\text{CO}_2$  reduction is how radical character is calculated to be delocalized predominantly across the phenolate-side of the  $\text{Me}_2\text{OQN}^{\text{–}}$  ring ( $\rho_{\text{Me}_2\text{OQN}} = 0.88$ ) with just a weak contribution from the formal  $\text{Re}^{\text{II}}$  ( $\rho_{\text{Re}} = 0.05$ ) oxidation state. This ligand-based oxidation is really triggered by protonation of the **[2-Re-CO<sub>2</sub>]<sup>–</sup>** adduct ( $\rho_{\text{Re}} = 0.27$ ;  $\rho_{\text{CO}_2} = 0.59$ ) which still possesses the  $\text{Me}_2\text{OQN}^{\text{–}}$  ligand in its native anionic state (Fig. 12).

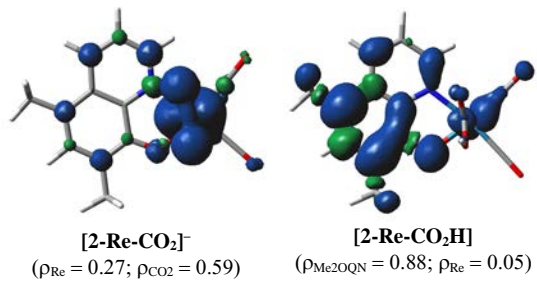
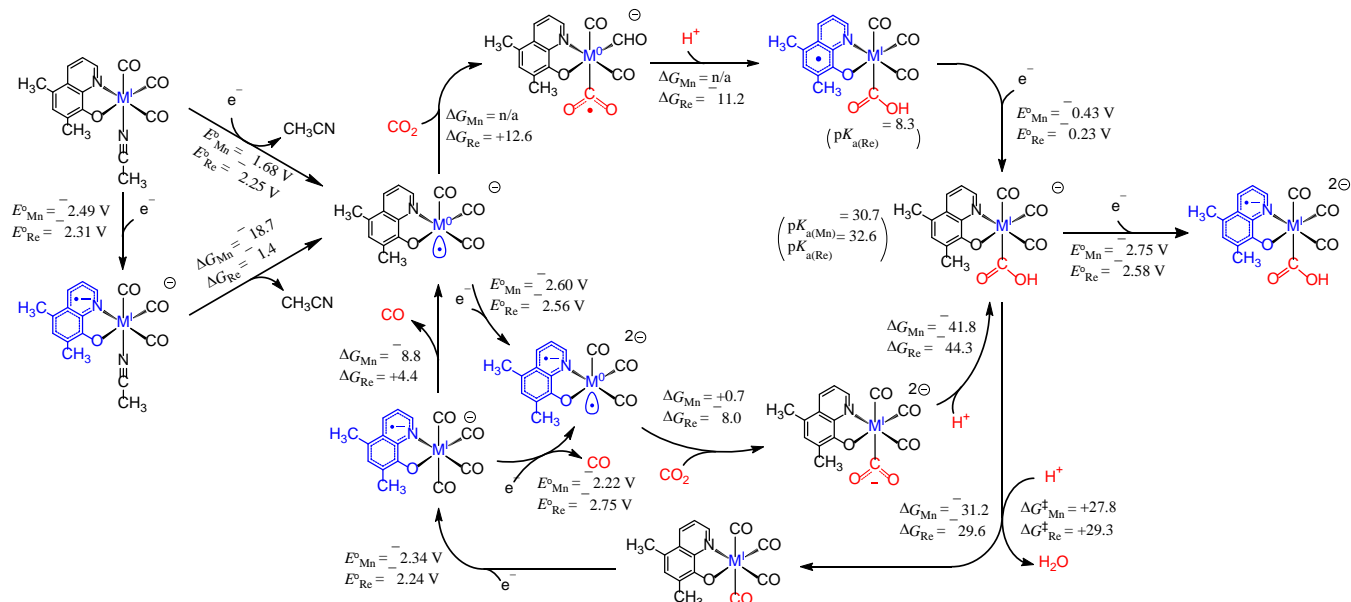


Figure 12. Spin density plots (isofactor = 0.001) computed at the M06 level of theory illustrating the significant contribution of the one-electron oxidized  $\text{Me}_2\text{OQN}^{\text{–}}$  ligand to the **[2-M-CO<sub>2</sub>H]** catalytic intermediate in contrast to its **[2-Re-CO<sub>2</sub>]<sup>–</sup>** precursor.

A facile reduction ( $E^\circ = –0.23$  V) is then predicted to regenerate the native  $\text{Me}_2\text{OQN}^{\text{–}}$  ligand oxidation state to result in the formation of **[2-Re-CO<sub>2</sub>H]<sup>–</sup>**. The computed energetics indicate that subsequent protonation resulting in C–OH bond cleavage is rate-limiting ( $\Delta G^\ddagger = 29.3$  kcal/mol) while the following one-electron reduction step to form **[2-Re-CO]<sup>–</sup>** is quite facile. In the case of the **[2-Mn-MeCN]** pre-catalyst, further reduction of the one-electron reduced intermediate, **[2-Mn]<sup>–</sup>**, to **[2-Mn]<sup>2–</sup>** is required for  $\text{CO}_2$  binding ( $\Delta G = 0.7$  kcal/mol), which upon protonation ( $\Delta G = –41.8$  kcal/mol) leads to formation of **[2-Mn-CO<sub>2</sub>H]<sup>–</sup>**. Next, C–OH bond cleavage assisted by water as the Brønsted acid is proposed to occur with a computed activation free energy,  $\Delta G^\ddagger = 27.8$  kcal/mol for **[2-Mn-CO<sub>2</sub>H]<sup>–</sup>**. Further one-electron reduction of the C–OH bond cleavage products, **[Re-CO]** and **[Mn-CO]**, followed by facile CO evolution, regenerates the active **[M]<sup>–</sup>** intermediate completing the catalytic cycle. For the **[1-Mn-MeCN]<sup>+</sup>** and **[1-Re-MeCN]<sup>+</sup>** pre-catalysts, C–OH bond cleavage exclusively proceeds via the *reduction-first pathway* in the present conditions, whereas this path is less likely to be accessible with **[2-Mn-MeCN]** and **[2-Re-MeCN]** due to the high overpotential requirements for the reduction of  $[\text{M-CO}_2\text{H}]^+$  to  $[\text{M-CO}_2\text{H}]^{2–}$  ( $E^\circ = –2.75$  V and –2.58 V for **[2-Mn-CO<sub>2</sub>H]<sup>–</sup>** and **[2-Re-CO<sub>2</sub>]<sup>–</sup>**, respectively). We have previously reported on the activation of this thermodynamically favorable *protonation-first pathway* utilizing Lewis base moieties in the second-coordination sphere of a Mn-bpy based pre-catalyst.<sup>3</sup> However, to the best of our knowledge, this is the first example of a Mn pre-catalyst providing access to the *protonation-first* pathway via inner coordination sphere effects. This behavior is not surprising when the electron-rich character of the  $\text{Me}_2\text{OQN}^{\text{–}}$  ligand is considered relative to bpy. Essentially, formation of the **[2-Mn-CO<sub>2</sub>H]<sup>–</sup>** intermediate precludes an additional reduction step as it already carries a negative charge upon its formation, facilitating direct access to the *protonation-first* pathway and avoiding an excessive overpotential. As a result, in comparison to **[1-Mn-MeCN]<sup>+</sup>** and **[1-Re-MeCN]<sup>+</sup>** pre-catalysts, the  $\text{Me}_2\text{OQN}^{\text{–}}$ -based pre-catalysts exhibit onset of catalytic current with the input of one less equivalent of electrons to access the rate-determining C–OH bond cleavage step. Moreover, the computed  $\Delta G^\ddagger$ s predict an order of magnitude faster CO evolution by **[2-Mn-**

**MeCN]** compared to **[2-Re-MeCN]**, in line with the experimentally observed TOFs.

**Scheme 3.** Proposed catalytic cycles for pre-catalysts **[2-Re-MeCN]** and **[2-Mn-MeCN]** including computed  $E^\circ$  (vs  $\text{Fc}^{+/0}$ ),  $\Delta G$  (kcal/mol) and  $\Delta G^\ddagger$  (kcal/mol) at the M06 level of theory.



## CONCLUSION

The electronic properties for both Mn and Re complexes of the general formula  $[\text{M}(\text{Me}_2\text{OQN})(\text{CO})_3(\text{CH}_3\text{CN})]$  have been presented and distinguished from their reference bpy-based analogues. The non-innocent  $\text{Me}_2\text{OQN}^-$  ligand imparts unique electrochemical properties to the **[2-Mn-MeCN]** and **[2-Re-MeCN]** pre-catalysts which make them particularly suited to electrocatalytic applications. In particular, under 1 atm of  $\text{CO}_2$  and in the presence of  $\text{H}_2\text{O}$  as a Brønsted acid, electrocatalytic  $\text{CO}_2$  reduction is demonstrated for both **[2-Mn-MeCN]** and **[2-Re-MeCN]** pre-catalysts. Onset of catalytic current for both **[2-Mn-MeCN]** and **[2-Re-MeCN]** is initiated with the input of one less equivalent of electrons relative to their bpy-based reference complexes,  $[\text{M}(\text{bpy})(\text{CO})_3(\text{CH}_3\text{CN})]^+$  ( $\text{M} = \text{Mn}$  or  $\text{Re}$ ). Utilizing spectroelectrochemical EPR, FTIR and computational analysis, in addition to the powerful technique of PR-TRIR spectroscopy, it was possible to narrow down the one-electron and two-electron reduced species relevant for the exhibition of  $\text{CO}_2$  reduction activity. In particular, for **[2-Re-MeCN]**, the formal  $\text{Me}_2\text{OQN}^{(\cdot-)}$  redox couple contributes towards each catalytic cycle in tandem with the formal  $\text{Re}^{1/0}$  redox couples by facilitating in-situ generation of the active catalyst and driving the rate-determining  $\text{C}-\text{OH}$  bond cleavage step upon just one-electron reduction of the pre-catalyst. In contrast, **[2-Mn-MeCN]** requires the input of a second electron to activate the catalyst. However, the coulombic

influence of the  $\text{Me}_2\text{OQN}^-$  ligand precludes the need for an additional overpotential associated with the *reduction-first* pathway, facilitating a *protonation-first*  $\text{CO}_2$  reduction pathway for both **[2-Mn-MeCN]** and **[2-Re-MeCN]** pre-catalysts.

## EXPERIMENTAL SECTION

### Materials and Methods

The following chemicals were purchased from Sigma Aldrich; bromopentacarbonylmanganese(I) (98%), silver trifluoromethanesulfonate (>99%), tetrabutylammonium hexafluorophosphate (>99%), potassium carbonate (>99%), 2,2,2-trifluoroethanol (>99%), tetrahydrofuran (anhydrous, 99.9%), hexane (ACS reagent grade, 99%), acetonitrile (ACS reagent grade, >99.5%). Tetrabutylammonium hexafluorophosphate was recrystallized thrice from ethanol and dried under vacuum prior to electrolyte preparation. The water content in ACS reagent grade acetonitrile was confirmed by Karl-Fisher titration to be 0.17 M (0.3%). Steady-state FTIR spectra were recorded on a Thermo Nicolet 670 FTIR spectrophotometer in spectrophotometric grade acetonitrile. NMR spectra were recorded on an Agilent spectrometer operated at 399.80 MHz for  $^1\text{H}$  nuclei.  $\text{CD}_3\text{CN}$  was used as received from Sigma Aldrich and its residual  $^1\text{H}$  solvent signal ( $\delta = 1.94 \text{ ppm}$ )<sup>44</sup> used as an internal reference for reporting the chemical shift. Voltammetry and bulk electrolysis were carried out on a CH Instruments 620E potentiostat. A

custom three electrode cell was used for both voltammetry and bulk electrolysis experiments allowing airtight introduction of working, counter and reference electrodes as well as septa for gas purging. For cyclic voltammetry, glassy carbon (3 mm diameter) and Pt wire were used as working and counter electrodes, respectively, with 0.1 M  $[\text{Bu}_4\text{N}][\text{PF}_6]$  in spectrophotometric grade acetonitrile as the supporting electrolyte. A non-aqueous reference electrode was used to minimize ohmic potential drop at the solvent interface. This consisted of a Ag wire in 0.10 M  $[\text{Bu}_4\text{N}][\text{PF}_6]$  acetonitrile supporting electrolyte isolated by a Vycor frit and was calibrated in-situ using the ferricinium/ferrocene redox couple as a pseudo reference. Redox potentials ( $E$ ) were determined from cyclic voltammetry as  $(E_{\text{pa}} + E_{\text{pc}})/2$ , where  $E_{\text{pa}}$  and  $E_{\text{pc}}$  are the anodic and cathodic peak potentials respectively. Where  $E$  could not be calculated due to irreversible behavior,  $E_{\text{pc}}$  or  $E_{\text{pa}}$  are reported accordingly. For  $\text{CO}_2$  concentration dependent studies, gas cylinders were ordered from Airgas containing pre-mixed ratios of Ar: $\text{CO}_2$  (100:0, 80:20, 60:40, 50:50, 40:60, 20:80, 0:100).

#### Controlled potential electrolysis & product quantification

For controlled potential bulk electrolysis experiments, a vitreous carbon (Structure Probe, Inc.) working electrode soldered to a copper wire was used. A Pt gauze counter electrode was used, isolated from the main compartment by a fine porosity Vycor tube+frit to minimize resistance. Gas chromatography data were recorded on a custom Shimadzu GC-2014 instrument where a Ni “methanizer” catalyst was used to convert CO to  $\text{CH}_4$  prior to quantification of  $\text{CH}_4$  by the thermal conductivity detector.  $\text{H}_2$  was simultaneously monitored by a flame ionization detector during the same injection. The GC was precalibrated for CO and  $\text{H}_2$  quantification by mimicking bulk electrolysis conditions (i.e. 5 mL supporting electrolyte in the same cell, with electrodes, under 1 atm  $\text{CO}_2$ ). Standard curves for  $\text{H}_2$  and CO were generated using this cell where known volumes of the analyte gas ( $\text{H}_2$  or CO) were injected and the solution stirred for 30 min to allow equilibration of the analyte between the electrolyte and headspace prior to GC injection. Formate analysis following bulk electrolysis was completed using a Dionex Aquion instrument using a Dionex IonPac AS22 (4 x 250 mm) anion column and Dionex AERS 500 Carbonate (4 mm) electrolytically regenerated suppressor. Samples were prepared for analysis by diluting an aliquot of the bulk electrolysis solution by a factor of ten in deionized water. Filtration to remove insoluble  $[\text{Bu}_4\text{N}][\text{PF}_6]$  electrolyte was required using a PVDF 0.22  $\mu\text{m}$  syringe filter. The diluent and mobile phase consisted of a sodium carbonate:bicarbonate (4.5:1.4) solution run at 0.70 mL/min at room temperature. The formate peak was observed at 6.23 min and integrated to quantify the concentration of formic acid produced in reference to a standard calibration curve.

#### Synthesis

**[Mn(Me<sub>2</sub>OQN)(CO)<sub>3</sub>(THF)]** To a microwave vial, ~3 mL of dry THF was left to purge gently with argon. To this vial, the ligand, 5,7-dimethyl-8-hydroxyquinoline (63 mg, 0.36 mmol) was added with a three-fold excess of  $\text{K}_2\text{CO}_3$  (150 mg, 1.09 mmol). This reaction solution was left to stir

for approximately 1 minute under argon. The manganese starting material, bromopentacarbonyl manganese(I) (100 mg, 0.36 mmol), was then added. The reaction vial was sealed quickly and irradiated at 60°C for approximately 1 hour. Upon cooling, the reaction mixture, a bright orange-red solution, was filtered through a small plug of alumina, removing the insoluble base. Recrystallization with hexanes yielded analytically pure product as a shiny yellow solid in 28% yield. FTIR (CH<sub>3</sub>CN)  $\nu(\text{CO})$ : 2032, 1938, 1915  $\text{cm}^{-1}$ . <sup>1</sup>H-NMR (CD<sub>3</sub>CN)  $\delta$ : 2.34 (3H, s), 2.51 (3H, s), 7.20 (1H, s), 7.46 (1H, dd,  $J_1$  = 4 Hz,  $J_2$  = 8 Hz), 8.37 (1H, dd,  $J_1$  = 2 Hz,  $J_2$  = 4 Hz), 8.98 (1H, dd,  $J_1$  = 2 Hz,  $J_2$  = 4 Hz). Anal. Calcd. for C<sub>18</sub>H<sub>18</sub>MnNO<sub>5</sub>: C, 56.41; H, 4.73; N, 3.65. Found: C, 56.82; H, 4.89; N, 3.48.

#### Electron paramagnetic resonance (EPR) spectroscopy

EPR spectra at X-band frequency (ca. 9.5 GHz) were obtained with a Magnetech MS-5000 benchtop EPR spectrometer equipped with a rectangular TE 102 cavity. The measurements were carried out in synthetic quartz glass tubes. For EPR spectroelectrochemistry a three-electrode setup was employed using two Teflon-coated platinum wires (0.005" bare, 0.008" coated) as working (or a Teflon-coated gold wire (0.003" bare, 0.0055" coated) as working electrode) and counter electrode and a Teflon-coated silver wire (0.005" bare, 0.007" coated) as a pseudoreference electrode. All spectra were recorded at 77 K in 0.1 M  $[\text{Bu}_4\text{N}][\text{PF}_6]$  acetonitrile following controlled potential electrolysis. Spectral simulations were performed with EasySpin 5.1.4 and MatLab R2012a.

#### Pulse Radiolysis Step-Scan FTIR Experiments

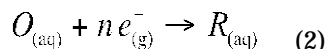
Pulse radiolysis experiments were conducted at the 2 MeV Van de Graaff (VdG) electron accelerator located in the Chemistry Division at Brookhaven National Laboratory. A commercial step-scan FTIR spectrometer (Bruker, Vertex 80v) equipped with an external fast risetime HgCdTe IR detector was placed on an air-stabilized optical bench close to the VdG's electron beam line exit window, with the electron beam passing directly through a homemade, air-tight IR flow cell (0.7 mm pathlength) equipped with 0.5 mm thick CaF<sub>2</sub> windows. A 25 mL CH<sub>3</sub>CN solution containing 1.5 mM of the Mn complex and 0.025 M tetrabutylammonium formate (synthesized according to a reported procedure<sup>40</sup>) was prepared inside a glovebox and placed into a sealed reservoir vessel. The vessel was then inserted into a gas-tight recirculating flow system containing a magnetically-coupled gear pump (Micropump). The tubing was evacuated and refilled with argon several times before saturating the solution with 2 atm argon and flowing. The VdG can produce electron pulses of increasing dose by increasing the electron pulsewidth up to a maximum of 5  $\mu\text{s}$ . In these experiments, we used 500 ns electron pulses at a repetition rate of 5 Hz. Since our experiments were not quantitative, we did not measure the absorbed dose. The time-resolved step-scan FTIR measurements were performed in a manner similar to those previously reported<sup>45</sup> for laser flash photolysis, except in this case a digital delay generator (Stanford Research Systems, DG535) was used to trigger the electron pulses in synchronization with the data collection. A preamplifier

built into the IR detector was used to amplify the detector signal prior to digitization. In a typical experiment, data were collected at 6 cm<sup>-1</sup> spectral resolution with an optical band pass filter that resulted in 255 interferogram mirror positions. 16 averages were acquired at each mirror position, leading to a total of 4080 electron pulses impinging on the flowing sample. FTIR spectra recorded after the experiment showed very little overall sample decomposition (< 5 %).

## Computational Methods

**Density functional theory.** All geometries were fully optimized at the M06-L<sup>46</sup> and M06 levels of density functional theory<sup>47-49</sup> with the SMD continuum solvation model<sup>50</sup> for acetonitrile as solvent using the Stuttgart [8s7p6d2f | 6s5p3d1f] ECP10MDF contracted pseudopotential basis set<sup>51</sup> on Mn, the Stuttgart [8s7p6d2f | 6s5p3d2f] ECP60MWB contracted pseudopotential basis set<sup>52</sup> on Re and the 6-31G(d) basis set on all other atoms.<sup>53</sup> Non-analytical integrals were evaluated using the integral=grid=ultrafine option as implemented in the Gaussian 16 software package.<sup>54</sup> The nature of all stationary points was verified by analytic computation of vibrational frequencies, which were also used for the computation of zero-point vibrational energies, molecular partition functions, and for determining the reactants and products associated with each transition-state structure (by following the normal modes associated with imaginary frequencies). Partition functions were used in the computation of 298 K thermal contributions to the free energy employing the usual ideal-gas, rigid-rotator, harmonic oscillator approximation.<sup>55</sup> Free-energy contributions were added to single-point, SMD-solvated M06-L and M06 electronic energies computed at the optimized geometries obtained with the initial basis with the SDD basis set on Mn and Re, and the larger 6-311+G(2df,p) basis set on all other atoms to arrive at final, composite free energies.

**Solvation and standard reduction potentials.** As mentioned above, solvation effects for acetonitrile were accounted for by using the SMD continuum solvation model. A 1 M standard state was used for all species in solution (except for acetonitrile as solvent for which the standard state was assigned as 19.14 M). Thus, the free energy in solution is computed as the 1 atm gas-phase free energy, plus an adjustment for the 1 atm to 1 M standard-state concentration change of  $RT \ln (24.5)$ , or 1.9 kcal/mol, plus the 1 M to 1 M transfer (solvation) free energy computed from the SMD model. Standard reduction potentials were calculated for various possible redox couples to assess the energetic accessibility of different intermediates at various oxidation states. For a redox reaction of the form



where  $O$  and  $R$  denote the oxidized and reduced states of the redox couple, respectively, and  $n$  is the number of electrons involved in redox reaction, the reduction potential  $E_{O|R}^o$  relative to SCE was computed as

$$E_{O|R}^o = -\frac{\Delta G_{O|R}^o}{nF} - \Delta E_{ref}^o \quad (3)$$

where  $\Delta G_{O|R}^o$  is the free energy change associated with eq. 2 (using Boltzmann statistics for the electron) and  $\Delta E_{ref}^o$  is taken as 0.141 V,<sup>56</sup> which is required for the conversion of calculated  $E_{O|R}^o$  versus normal hydrogen electrode (NHE) in aqueous solution ( $E_{NHE} = -4.281$  V)<sup>57</sup> to  $E_{O|R}^o$  versus the saturated calomel electrode (SCE) in acetonitrile ( $E_{SCE} = -4.422$  V).<sup>58</sup> We obtained reduction potentials referenced to the ferricenium/ferrocene couple by using a shift of -0.384 V from  $E_{O|R}^o$  vs SCE.

## ASSOCIATED CONTENT

### Supporting Information

NMR and FTIR spectra of **[2-Mn-MeCN]**, cyclic voltammetry, catalyst and CO<sub>2</sub> concentration dependence, TOF overlay plot, spectroelectrochemical EPR and FTIR, computational FTIR, spin-density plots and transition state geometries, complete reference # 54.

The Supporting Information is available free of charge on the ACS Publications website.

## AUTHOR INFORMATION

### Corresponding Authors

E-mail addresses:

jonathan.rochford@umb.edu (J. Rochford)

dcgrills@bnl.gov (D.C. Grills)

mzertem@bnl.gov (M.Z. Ertem)

### ORCID

Mehmed Z. Ertem: [0000-0003-1994-9024](https://orcid.org/0000-0003-1994-9024)

David C. Grills: [0000-0001-8349-9158](https://orcid.org/0000-0001-8349-9158)

Jonathan Rochford: [0000-0003-2397-9162](https://orcid.org/0000-0003-2397-9162)

### Notes

The authors declare no competing financial interests.

## ACKNOWLEDGMENT

J.R. thanks the National Science Foundation for support under grant number CHE-1301132. The work at BNL (D.C.G. and M.Z.E.), including use of the Van de Graaff facility of the BNL Accelerator Center for Energy Research (ACER), was supported by the U.S. Department of Energy

(DOE), Office of Basic Energy Sciences, Division of Chemical Sciences, Geosciences & Biosciences, under contract No. DE-SC0012704. K.T.N. is grateful to the DOE for an Office of Science Graduate Student Research (SCGSR) award. Some of this research used resources of the Center for Functional Nanomaterials (CFN) for the fabrication of optics for PR-TRIR experiments and computational mod-

eling studies. The CFN is a U.S. DOE Office of Science Facility at Brookhaven National Laboratory, operating under contract No. DE-SC0012704.

## REFERENCES

- Grills, D. C.; Ertem, M. Z.; McKinnon, M.; Ngo, K. T.; Rochford, J., *Mechanistic aspects of CO<sub>2</sub> reduction catalysis with manganese-based molecular catalysts*. *Coord. Chem. Rev.* **2018**, *374*, 173-217.
- Francke, R.; Schille, B.; Roemelt, M., *Homogeneously Catalyzed Electrocatalysis of Carbon Dioxide—Methods, Mechanisms, and Catalysts*. *Chem. Rev.* **2018**, *118*, 4631-4701.
- Ngo, K. T., et al., *Turning on the Protonation-First Pathway for Electrocatalytic CO<sub>2</sub> Reduction by Manganese Bipyridyl Tricarbonyl Complexes*. *J. Am. Chem. Soc.* **2017**, *139*, 2604-2618.
- Franco, F.; Pinto, M. F.; Royo, B.; Lloret-Fillol, J., *A Highly Active N-Heterocyclic Carbene Manganese(I) Complex for Selective Electrocatalytic CO<sub>2</sub> Reduction to CO*. *Angew. Chem. Int. Ed.* **2018**, *57*, 4603-4606.
- Walsh, J. J.; Neri, G.; Smith, C. L.; Cowan, A. J., *Electrocatalytic CO<sub>2</sub> reduction with a membrane supported manganese catalyst in aqueous solution*. *Chem. Commun.* **2014**, *50*, 12698-12701.
- Reuillard, B., et al., *Tuning Product Selectivity for Aqueous CO<sub>2</sub> Reduction with a Mn(bipyridine)-pyrene Catalyst Immobilized on a Carbon Nanotube Electrode*. *J. Am. Chem. Soc.* **2017**, *139*, 14425-14435.
- Hawecker, J.; Lehn, J. M.; Ziessel, R., *Electrocatalytic Reduction of Carbon-Dioxide Mediated by Re(bipy)(CO)<sub>3</sub>Cl (Bipy=2,2'-Bipyridine)*. *J. Chem. Soc., Chem. Commun.* **1984**, 328-330.
- Hawecker, J.; Lehn, J. M.; Ziessel, R., *Photochemical and electrochemical reduction of carbon dioxide to carbon monoxide mediated by (2,2'-bipyridine)tricarbonylchlororhenium(I) and related complexes as homogeneous catalysts*. *Helv. Chim. Acta* **1986**, *69*, 1990-2012.
- Sullivan, B. P.; Bolinger, C. M.; Conrad, D.; Vining, W. J.; Meyer, T. J., *One-Electron and 2-Electron Pathways in the Electrocatalytic Reduction of CO<sub>2</sub> by fac-Re(2,2'-Bipyridine)(CO)<sub>3</sub>Cl*. *J. Chem. Soc., Chem. Commun.* **1985**, 1414-1415.
- Bourrez, M.; Molton, F.; Chardon-Noblat, S.; Deronzier, A., *Mn(bipyridyl)(CO)<sub>3</sub>Br : An Abundant Metal Carbonyl Complex as Efficient Electrocatalyst for CO<sub>2</sub> Reduction*. *Angew. Chem. Int. Ed.* **2011**, *50*, 9903-9906.
- Franco, F., et al., *A local proton source in a Mn(bpy-R)(CO)<sub>3</sub>Br -type redox catalyst enables CO<sub>2</sub> reduction even in the absence of Bronsted acids*. *Chem. Commun.* **2014**, *50*, 14670-14673.
- Rao, G. K.; Pell, W.; Korobkov, I.; Richeson, D., *Electrocatalytic reduction of CO<sub>2</sub> using Mn complexes with unconventional coordination environments*. *Chem. Commun.* **2016**, *52*, 8010-8013.
- Franco, F., et al., *Local Proton Source in Electrocatalytic CO<sub>2</sub> Reduction with [Mn(bpy-R)(CO)<sub>3</sub>Br] Complexes*. *Chem. Eur. J.* **2017**, *23*, 4782-4793.
- Riplinger, C.; Sampson, M. D.; Ritzmann, A. M.; Kubiak, C. P.; Carter, E. A., *Mechanistic Contrasts between Manganese and Rhenium Bipyridine Electrocatalysts for the Reduction of Carbon Dioxide*. *J. Am. Chem. Soc.* **2014**, *136*, 16285-16298.
- Riplinger, C.; Carter, E. A., *Influence of Weak Brønsted Acids on Electrocatalytic CO<sub>2</sub> Reduction by Manganese and Rhenium Bipyridine Catalysts*. *ACS Catal.* **2015**, *5*, 900-908.
- Agarwal, J., et al., *NHC-Containing Manganese(I) Electrocatalysts for the Two-Electron Reduction of CO<sub>2</sub>*. *Angew. Chem. Int. Ed.* **2014**, *53*, 5152-5155.
- Stanton III, C. J.; Vandezande, J. E.; Majetich, G. F.; Schaefer III, H. F.; Agarwal, J., *Mn-NHC Electrocatalysts: Increasing π Acidity Lowers the Reduction Potential and Increases the Turnover Frequency for CO<sub>2</sub> Reduction*. *Inorg. Chem.* **2016**, *55*, 9509-9512.
- Spall, S. J. P., et al., *Manganese Tricarbonyl Complexes with Asymmetric 2-Iminopyridine Ligands: Toward Decoupling Steric and Electronic Factors in Electrocatalytic CO<sub>2</sub> Reduction*. *Inorg. Chem.* **2016**, *55*, 12568-12582.
- Matsuzaki, R.; Suzuki, S.; Yamaguchi, K.; Fukui, T.; Tanizawa, K., *Spectroscopic studies on the mechanism of the TOPA quinone generation in bacterial monoamine oxidase*. *Biochemistry* **1995**, *34*, 4524-4530.
- Tabuchi, K., et al., *Reactions of Copper(II)-Phenol Systems with O<sub>2</sub>: Models for TPQ Biosynthesis in Copper Amine Oxidases*. *Inorg. Chem.* **2011**, *50*, 1633-1647.
- Vu, V. V.; Ngo, S. T., *Copper active site in polysaccharide monooxygenases*. *Coord. Chem. Rev.* **2018**, *368*, 134-157.
- Turner, N. J., *Enantioselective Oxidation of C-O and C-N Bonds Using Oxidases*. *Chem. Rev.* **2011**, *111*, 4073-4087.
- Jørgensen, C. K., *Differences between the four halide ligands, and discussion remarks on trigonal-bipyramidal complexes, on oxidation states, and on diagonal elements of one-electron energy*. *Coord. Chem. Rev.* **1966**, *1*, 164-178.
- Kaim, W., *Manifestations of Noninnocent Ligand Behavior*. *Inorg. Chem.* **2011**, *50*, 9752-9765.
- Allgeier, A. M.; Mirkin, C. A., *Ligand design for electrochemically controlling stoichiometric and catalytic reactivity of transition metals*. *Angew. Chem., Int. Ed.* **1998**, *37*, 895-908.
- Chaudhuri, P.; Wieghardt, K., *Phenoxy radical complexes*. *Prog. Inorg. Chem.* **2001**, *50*, 151-216.
- Muckerman, J. T.; Polyansky, D. E.; Wada, T.; Tanaka, K.; Fujita, E., *Water Oxidation by a Ruthenium Complex with Noninnocent Quinone Ligands: Possible Formation of an O-O Bond at a Low Oxidation State of the Metal*. *Inorg. Chem.* **2008**, *47*, 1787-1802.
- Lyaskovskyy, V.; de Bruin, B., *Redox Non-Innocent Ligands: Versatile New Tools to Control Catalytic Reactions*. *ACS Catal.* **2012**, *2*, 270-279.
- van der Meer, M., et al., *(Electro)catalytic C-C bond formation reaction with a redox-active cobalt complex*. *Chem. Commun.* **2014**, *50*, 11104-11106.
- Lacy, D. C.; McCrory, C. C. L.; Peters, J. C., *Studies of Cobalt-Mediated Electrocatalytic CO<sub>2</sub> Reduction Using a Redox-Active Ligand*. *Inorg. Chem.* **2014**, *53*, 4980-4988.
- Costentin, C.; Saveant, J. M.; Tard, C., *Ligand "noninnocence" in coordination complexes vs. kinetic, mechanistic, and selectivity issues in electrochemical catalysis*. *Proc. Natl. Acad. Sci. U.S.A.* **2018**, *115*, 9104-9109.
- Scheiring, T.; Klein, A.; Kaim, W., *EPR study of paramagnetic rhenium(I) complexes (bpy(center dot-))Re(CO)<sub>3</sub>X relevant to the mechanism of electrocatalytic CO<sub>2</sub> reduction*. *J. Chem. Soc., Perkin Trans. 2* **1997**, 2569-2571.
- Zhao, H. C., et al., *Investigation of Monomeric versus Dimeric fac-Rhenium(I) Tricarbonyl Systems Containing the*

*Noninnocent 8-Oxyquinolate Ligand. Organometallics* **2013**, *32*, 1832-1841.

34. Torralba-Peñalver, E.; Luo, Y.; Compain, J.-D.; Chardon-Noblat, S.; Fabre, B., *Selective Catalytic Electroreduction of CO<sub>2</sub> at Silicon Nanowires (SiNWs) Photocathodes Using Non-Noble Metal-Based Manganese Carbonyl Bipyridyl Molecular Catalysts in Solution and Grafted onto SiNWs. ACS Catal.* **2015**, *5*, 6138-6147.

35. Kaim, W., *The Shrinking World of Innocent Ligands: Conventional and Non-Conventional Redox-Active Ligands. Eur. J. Inorg. Chem.* **2012**, 343-348.

36. Costentin, C.; Drouet, S.; Robert, M.; Savéant, J.-M., *A Local Proton Source Enhances CO<sub>2</sub> Electroreduction to CO by a Molecular Fe Catalyst. Science* **2012**, *338*, 90-94.

37. Costentin, C.; Passard, G.; Savéant, J.-M., *Benchmarking of Homogeneous Electrocatalysts: Overpotential, Turnover Frequency, Limiting Turnover Number. J. Am. Chem. Soc.* **2015**, *137*, 5461-5467.

38. Grills, D. C.; Polyansky, D. E.; Fujita, E., *Application of Pulse Radiolysis to Mechanistic Investigations of Catalysis Relevant to Artificial Photosynthesis. ChemSusChem* **2017**, *10*, 4359-4373.

39. Grills, D. C.; Lymar, S. V., *Radiolytic formation of the carbon dioxide radical anion in acetonitrile revealed by transient IR spectroscopy. Phys. Chem. Chem. Phys.* **2018**, *20*, 10011-10017.

40. Grills, D. C., et al., *Mechanism of the Formation of a Mn-Based CO<sub>2</sub> Reduction Catalyst Revealed by Pulse Radiolysis with Time-Resolved Infrared Detection. J. Am. Chem. Soc.* **2014**, *136*, 5563-5566.

41. Grills, D. C., et al., *Development of nanosecond time-resolved infrared detection at the LEAF pulse radiolysis facility. Rev. Sci. Instrum.* **2015**, *86*, 044102.

42. Sampson, M. D., et al., *Manganese Catalysts with Bulky Bipyridine Ligands for the Electrocatalytic Reduction of Carbon Dioxide: Eliminating Dimerization and Altering Catalysis. J. Am. Chem. Soc.* **2014**, *136*, 5460-5471.

43. Sampson, M. D.; Kubiak, C. P., *Manganese Electrocatalysts with Bulky Bipyridine Ligands: Utilizing Lewis Acids To Promote Carbon Dioxide Reduction at Low Overpotentials. J. Am. Chem. Soc.* **2016**, *138*, 1386-1393.

44. Fulmer, G. R., et al., *NMR Chemical Shifts of Trace Impurities: Common Laboratory Solvents, Organics, and Gases in Deuterated Solvents Relevant to the Organometallic Chemist. Organometallics* **2010**, *29*, 2176-2179.

45. Grills, D. C.; van Eldik, R.; Muckerman, J. T.; Fujita, E., *Direct Measurements of Rate Constants and Activation Volumes for the Binding of H<sub>2</sub>, D<sub>2</sub>, N<sub>2</sub>, C<sub>2</sub>H<sub>4</sub>, and CH<sub>3</sub>CN to W(CO)<sub>3</sub>(PCy<sub>3</sub>)<sub>2</sub>: Theoretical and Experimental Studies with Time-Resolved Step-Scan FTIR and UV-Vis Spectroscopy. J. Am. Chem. Soc.* **2006**, *128*, 15728-15741.

46. Zhao, Y.; Truhlar, D. G., *A new local density functional for main-group thermochemistry, transition metal bonding, thermochemical kinetics, and noncovalent interactions. J. Chem. Phys.* **2006**, *125*, 194101.

47. Zhao, Y.; Truhlar, D. G., *The M06 suite of density functionals for main group thermochemistry, thermochemical kinetics, noncovalent interactions, excited states, and transition elements: two new functionals and systematic testing of four M06-class functionals and 12 other functionals. Theor. Chem. Acc.* **2008**, *120*, 215-241.

48. Zhao, Y.; Truhlar, D. G., *Density Functionals with Broad Applicability in Chemistry. Acc. Chem. Res.* **2008**, *41*, 157-167.

49. Zhao, Y.; Truhlar, D. G., *The Minnesota Density Functionals and their Applications to Problems in Mineralogy and Geochemistry. Rev. Mineral Geochem.* **2010**, *71*, 19-37.

50. Marenich, A. V.; Cramer, C. J.; Truhlar, D. G., *Universal Solvation Model Based on Solute Electron Density and on a Continuum Model of the Solvent Defined by the Bulk Dielectric Constant and Atomic Surface Tensions. J. Phys. Chem. B* **2009**, *113*, 6378-6396.

51. Dolg, M.; Wedig, U.; Stoll, H.; Preuss, H., *Energy-adjusted ab initio pseudopotentials for the first row transition elements. J. Chem. Phys.* **1987**, *86*, 866-872.

52. Andrae, D.; Häußermann, U.; Dolg, M.; Stoll, H.; Preuß, H., *Energy-adjusted ab initio pseudopotentials for the second and third row transition elements. Theor. Chim. Acta* **1990**, *77*, 123-141.

53. Hehre, W. J.; Radom, L.; Schleyer, P. v. R.; Pople, J. A., *Ab Initio Molecular Orbital Theory*. Wiley: New York, 1986.

54. Frisch, M. J., et al. *Gaussian 16 Rev. A.03*, Wallingford, CT, 2016.

55. Cramer, C. J., *Essentials of Computational Chemistry: Theories and Models*. 2nd ed.; John Wiley & Sons: Chichester, 2004; p 385-427.

56. Keith, J. A.; Grice, K. A.; Kubiak, C. P.; Carter, E. A., *Elucidation of the Selectivity of Proton-Dependent Electrocatalytic CO<sub>2</sub> Reduction by fac-Re(bpy)(CO)<sub>3</sub>Cl. J. Am. Chem. Soc.* **2013**, *135*, 15823-15829.

57. Kelly, C. P.; Cramer, C. J.; Truhlar, D. G., *Aqueous solvation free energies of ions and ion-water clusters based on an accurate value for the absolute aqueous solvation free energy of the proton. J. Phys. Chem. B* **2006**, *110*, 16066-16081.

58. Isse, A. A.; Gennaro, A., *Absolute Potential of the Standard Hydrogen Electrode and the Problem of Interconversion of Potentials in Different Solvents. J. Phys. Chem. B* **2010**, *114*, 7894-7899.